



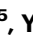

# A shared central thalamus mechanism underlying diverse recoveries in disorders of consciousness

Received: 18 November 2024

Accepted: 10 October 2025

Published online: 24 November 2025

 Check for updates

Haoran Zhang <sup>1,2,3</sup>, Qianqian Ge <sup>4</sup>, Xiao Liu <sup>5</sup>, Yuanyuan Dang<sup>6</sup>, Long Xu<sup>4</sup>, Yutong Zhuang<sup>4</sup>, Si Wu <sup>5</sup>, Steven Laureys <sup>7,8,9</sup> , Jianghong He <sup>4</sup>  & Shan Yu <sup>1,2,3</sup> 

Disorders of consciousness (DoC) encompass a range of states characterized by prolonged altered awareness due to heterogeneous brain damage and are associated with highly diverse prognoses. However, the neural mechanisms underlying such diverse recoveries in DoC remain unclear. To address this issue, we analyzed direct recordings from the central thalamus (CeTh), a key hub in arousal regulation, in a series of 23 DoC patients receiving deep brain stimulation treatment (CeTh-DBS). We identified a core set of electrophysiological features of the CeTh, particularly those of the theta rhythm. These features could account for individual recovery outcomes across highly varied etiologies (trauma, brainstem hemorrhage, and anoxia), and across clinical baselines and patient ages. CeTh activities also identified two subgroups of patients with recovery potential, including those with poor initial clinical manifestations but who eventually exhibited functional recovery. A biophysical model further revealed the neurodynamics of the theta rhythm in the CeTh across different brain states correlating with varying consciousness levels. These findings uncover a shared CeTh mechanism underlying diverse recoveries in DoC.

Disorders of consciousness (DoC) encompass conditions characterized by impaired arousal and awareness due to severe brain damage, including coma<sup>1</sup>, unresponsive wakefulness syndrome/vegetative state (UWS/VS)<sup>2–4</sup>, and minimally conscious state (minus/plus, MCS–/MCS+)<sup>5–7</sup>. These conditions impose significant challenges to patients' families and the healthcare system due to the difficulty of managing prolonged bedridden status, demanding care, and low rates of functional recovery<sup>3,8</sup>. Importantly, the causes and extent of

brain damage leading to DoC are highly heterogeneous, including trauma, stroke, and anoxia, and ranging from focal injuries such as brainstem hemorrhage (BSH) to extensive lesions across the cortex<sup>9</sup>. Heterogeneous etiologies are associated with varying prognoses. For instance, individuals with traumatic injuries often exhibit better outcomes compared to those with anoxic brain injuries<sup>4,8,10–13</sup>. Factors such as the clinical baseline (e.g., UWS, MCS), age, and time since damage onset further contribute to variations in prognoses<sup>3,12–15</sup>.

<sup>1</sup>Laboratory of Brain Atlas and Brain-inspired Intelligence, Institute of Automation, Chinese Academy of Sciences, Beijing, China. <sup>2</sup>School of Future Technology, University of Chinese Academy of Sciences, Beijing, China. <sup>3</sup>State Key Laboratory of Brain Cognition & Brain-inspired Intelligence, Institute of Automation, Chinese Academy of Sciences, Beijing, China. <sup>4</sup>Department of Neurosurgery, Beijing Tiantan Hospital, Capital Medical University, Beijing, China. <sup>5</sup>School of Psychological and Cognitive Sciences, IDG/McGovern Institute for Brain Research, Peking-Tsinghua Center for Life Sciences, Center for Quantitative Biology, Academy for Advanced Interdisciplinary Studies, Peking University, Beijing, China. <sup>6</sup>Department of Neurosurgery, The First Medical Center of Chinese PLA General Hospital, Beijing, China. <sup>7</sup>CERVO Brain Research Centre, Laval University, Québec, QC, Canada. <sup>8</sup>Coma Science Group, GIGA Consciousness Research Unit, Liège University Hospital, Liège, Belgium. <sup>9</sup>International Consciousness Science Institute, Hangzhou Normal University, Hangzhou, China.  e-mail: [steven.laureys@cervo.ulaval.ca](mailto:steven.laureys@cervo.ulaval.ca); [he\\_jianghong@sina.cn](mailto:he_jianghong@sina.cn); [shan.yu@nlpr.ia.ac.cn](mailto:shan.yu@nlpr.ia.ac.cn)

However, the neural mechanism underlying such diverse recoveries in various clinical factors remains unclear.

Non-invasive studies using fMRI and EEG have suggested that the status of macroscopic brain networks, including the default mode network, executive control network, and thalamocortical connectivity integrity<sup>16–18</sup>, as well as neuronal oscillation and synchrony within the fronto-parietal region<sup>19–21</sup>, may correlate with DoC recovery. However, the role of the thalamus, particularly the central thalamus (CeTh), in functional recovery in DoC remains incompletely understood as its activities cannot be assessed with high resolution using noninvasive methods. As a bidirectional hub in arousal regulation, the CeTh receives inputs from the brainstem through the ascending reticular activating system (ARAS)<sup>22–24</sup> and sends broad projections modulating the frontal-striatal system<sup>14,22,23,25–30</sup>. Despite its critical role, direct recordings from the CeTh in DoC patients are scarce, with studies limited to a few cases or only coarse group-level statistical comparisons<sup>31–33</sup>.

Here, we retrospectively analyze 23 intraoperative microelectrode recordings collected during DBS procedures performed in DoC patients at our centers. These patients have heterogeneous etiologies—trauma ( $n = 6$ ), BSH ( $n = 8$ ), and anoxia ( $n = 9$ )—but all have relatively well-preserved brain structures (Supplementary Table 1 and Supplementary Fig. 1). Among them, eight patients demonstrate consciousness recovery (CR) after one year of CeTh-DBS treatment, characterized by the regaining of language processing capabilities. We investigate two modalities of CeTh activity—neuronal spiking and multiunit activity (MUA)—to identify key electrophysiological features of CeTh that can characterize individual recovery outcomes in response to DBS-treatment. We show that the CeTh activities, particularly those related to theta band oscillations, play a crucial role in functional recovery across various clinical factors in DoC.

## Results

### CeTh features enable individualized prognosis for DoC

All patients underwent deep brain stimulation (DBS) treatment targeting the CeTh (Fig. 1a). We analyzed two modalities of CeTh activity: neuronal spiking and multiunit activity (MUA) (Fig. 1b). Compared to the local field potential, which is the low-frequency component reflecting synaptic inputs and could experience volume conduction<sup>34</sup>, MUA captures high-frequency signals that provide more localized information on population neuronal outputs within a range of approximately 100–200  $\mu\text{m}$  radius from the recording electrode<sup>35–37</sup>, demonstrating unique strength in characterizing activities of small nuclei<sup>38,39</sup>. Leveraging these two modalities, we examined a total of 34 electrophysiological features to characterize the CeTh state, covering multifaceted properties including the discharge properties of single neurons<sup>26,40</sup>, synchronization among neuron populations<sup>38,39,41</sup>, coherence between the activity of individual neurons and that of population<sup>26,27,42,43</sup>, and background noise levels<sup>44</sup>.

We found that the electrophysiological features of the CeTh show redundancy, noise, and variable discrimination power (Fig. 1c, left). To identify features that best characterize the differences between consciousness recovery and non-recovery patients in response to CeTh-DBS<sup>17,21,45,46</sup>, we employed a machine learning pipeline to select the optimal feature combination (Supplementary Fig. 2a; see “Methods”). As a result, we identified a combination of four features (Fig. 1c, right) that characterized differences between patients who exhibited CR and those who did not (unCR) (Supplementary Fig. 3b–d and Fig. 1f)—a discrimination that unselected features failed to achieve (Supplementary Fig. 3a). These four features include: (1) MUA stability in the theta band (stab- $\theta$ ), which is associated with thalamic intermittent bursting patterns (see Fig. 1b for an example)<sup>47,48</sup>; (2) MUA power in the theta band (pow- $\theta$ ), measuring the amplitude of theta band oscillation of MUA; (3) spiking-MUA synchronization in the gamma band (sync- $\gamma$ ), measuring the synchronization of neuronal spiking and MUA

population fluctuation in the gamma band; and (4) MUA stability in the high gamma band (stab-h $\gamma$ ).

After identifying this key feature set, we conducted feature performance analysis: (1) The Permutation Test demonstrated that classification using these features significantly outperformed chance level (Fig. 1d), suggesting that the observed performance reflects electrophysiological patterns rather than overfitting to noise; (2) Feature contribution evaluation confirmed that all four features enhanced the model’s performance (Fig. 1e and Supplementary Table 4), showing progressive improvements in both accuracy and F1 score as features were sequentially added, suggesting that each feature meaningfully contributes to classification; (3) While our selected features achieved perfect discrimination between CR and unCR patients ( $N = 23$ ), we consider this result likely coincidental due to the limited sample size. As shown in Fig. 1f, several patients have decision values near the classification threshold, indicating relatively low classification confidence for these cases. This pattern suggests that with larger, more diverse samples, classification errors would naturally emerge. Importantly, our aim was not to develop a generalizable prediction model with perfect accuracy, but rather to identify key CeTh features that strongly characterize consciousness recovery differences.

### CeTh status provides a shared indicator of DoC recovery across diverse clinical factors

After identifying key features that characterize CeTh status, we developed a CeTh metric for DoC prognosis based on the model weights of the selected feature set (Fig. 1f, see also Eq. 13 in “Methods”). Using this CeTh metric, we then confirmed previous findings that diverse clinical factors, including diagnostic baselines<sup>3,11,12,14</sup>, ages<sup>13,15</sup>, and etiologies<sup>4,8,10–13</sup>, influence prognosis. We measured the CR rate across various groups defined by these clinical factors. A higher CR rate was observed in the MCS- group compared to the UWS group (Fig. 2a inset, Fisher’s Exact Test,  $p = 0.006$ , Cohen’s  $h = 1.35$ ). Similarly, the younger group demonstrated a higher CR rate compared to the older group (Fig. 2b inset, Fisher’s Exact Test,  $p = 0.006$ , Cohen’s  $h = 1.35$ ). Regarding etiology, the highest CR rate was observed in the trauma group—66.7% in trauma, 22.2% in BSH, and 25% in anoxia. However, the differences among three etiologic groups were not statistically significant (Fig. 2c inset, Fisher’s Exact Test,  $p = 0.250$ ). Importantly, we found that, across all these groups defined by clinical factors, the patients whose CeTh metric score was above a specific threshold eventually recovered (Fig. 2a–c). This indicates that the CeTh’s status is a key indicator of consciousness recovery in DoC across various clinical factors, suggesting that DoC recoveries share a common mechanism in which the CeTh plays a pivotal role.

Additionally, we examined etiological differences for each selected CeTh feature separately. Only pow- $\theta$  showed significant discrimination among etiologies (Fig. 2d, Kruskal–Wallis Test,  $p = 7.20 \times 10^{-4}$ ,  $\eta^2 = 0.515$ ). Post-hoc tests (Conover’s All-Pairs Rank Comparison Test) revealed significantly stronger pow- $\theta$  in the BSH group compared to anoxia ( $p = 1.72 \times 10^{-4}$ ) and in the trauma group compared to anoxia ( $p = 0.042$ ). Although there was a trend toward higher pow- $\theta$  in BSH compared to trauma, the difference was not significant ( $p = 0.056$ ).

To better understand the different CeTh statuses that may lead to varying prognoses after CeTh-DBS, we examined the differences that discriminate between the CR and unCR groups. The patient-similarity matrix based on the CeTh metric (Fig. 2e) shows that the intra-group similarity is significantly higher than the inter-group similarity (Wilcoxon Rank Sum Test,  $p = 1.98 \times 10^{-10}$ , Fig. 2f). In addition, intra-group similarity is significantly lower in the CR group than in the unCR group (Wilcoxon Rank Sum Test,  $p = 1.18 \times 10^{-4}$ , Fig. 2f), indicating that unCR patients exhibit more consistent electrophysiological patterns. Additionally, we analyzed activity patterns of the CeTh metric in the CR and

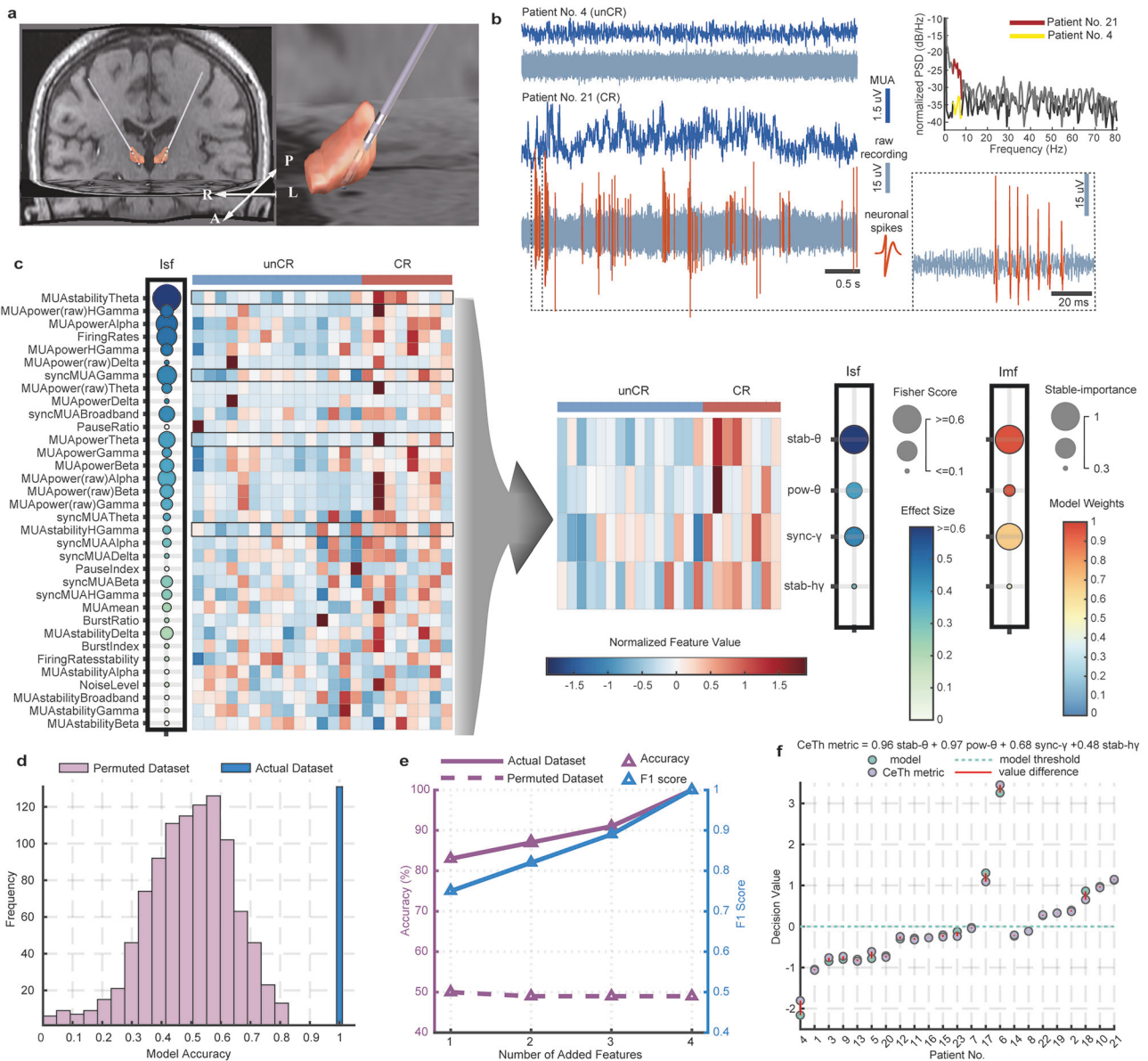


**Fig. 1 | Individualized prognosis for DoC using CeTh features.** **a** Magnetic resonance imaging (MRI) coronal view showing electrode placements in the bilateral central thalamus (CeTh) of an example patient (Patient No. 18), with an inset showing the left hemisphere electrode (L, left; R, right; A, anterior; P, posterior). **b** Visualization of electrophysiological signals extracted from the raw recording: neuronal spikes and multiunit activity (MUA). Examples from two patients are shown: Patient No. 4 (consciousness non-recovery, abbreviated as unCR) is characterized by a predominantly silent state, exhibiting only background activity, while Patient No. 21 (consciousness recovery, abbreviated as CR) displays intermittent bursting activity and corresponding unstable MUA activity. The normalized power spectrum (PSD) for the MUA signals of both patients is presented, with the theta band highlighted. **c** Electrophysiological profiles of the CeTh before and after feature selection: the left panel shows the distribution of 34 CeTh features across patients. The importance of Single-Feature (Isf) is indicated by the Fisher Score (circle size) and effect size (color intensity), illustrating the variability among individual features. The four selected features are highlighted with black borders and are further detailed in the right panel, including stability in theta band (MUstabilityTheta, abbreviated as stab- $\theta$ ), theta band power (MUpowerTheta, abbreviated as pow- $\theta$ ), spiking-MUA synchronization in the gamma band (syncMUGamma, abbreviated as sync- $\gamma$ ), stability in the high-gamma band (MUstabilityHGamma, abbreviated as stab-h $\gamma$ ). The importance in Multi-Feature Combination (Imf) represents the stable-importance index (circle size) and feature weights (color intensity) in the CeTh metric as shown in (f). **d** Permutation test: the accuracy achieved with the actual dataset and the distribution of accuracies from Permuted Dataset. **e** Feature contribution evaluation: progressive improvement in model accuracy and F1 score as features are sequentially added (with the sequence of stab- $\theta$ , pow- $\theta$ , sync- $\gamma$ , stab-h $\gamma$ , see “Methods”), contrasted with baseline performance near chance level (50%) in the permuted datasets. **f** Decision values for all 23 patients from both the machine learning model and the CeTh metric. Values above 0 are classified as consciousness recovery (CR), while values below 0 are classified as non-recovery (unCR). The dashed line represents the model’s classification threshold. Vertical connecting lines show the difference between each patient’s decision values as determined by the model and the CeTh metric. Source data are provided as a Source Data file.

unCR groups, respectively. Venn diagrams illustrate distinct feature distributions: CR patients demonstrated higher values across multiple features simultaneously (Fig. 2g), while unCR patients generally exhibited lower activity levels, with typically only a single feature showing high values (Fig. 2h).

(MUstabilityTheta, abbreviated as stab- $\theta$ ), theta band power (MUpowerTheta, abbreviated as pow- $\theta$ ), spiking-MUA synchronization in the gamma band (syncMUGamma, abbreviated as sync- $\gamma$ ), stability in the high-gamma band (MUstabilityHGamma, abbreviated as stab-h $\gamma$ ). The importance in Multi-Feature Combination (Imf) represents the stable-importance index (circle size) and feature weights (color intensity) in the CeTh metric as shown in (f). **d** Permutation test: the accuracy achieved with the actual dataset and the distribution of accuracies from Permuted Dataset. **e** Feature contribution evaluation: progressive improvement in model accuracy and F1 score as features are sequentially added (with the sequence of stab- $\theta$ , pow- $\theta$ , sync- $\gamma$ , stab-h $\gamma$ , see “Methods”), contrasted with baseline performance near chance level (50%) in the permuted datasets. **f** Decision values for all 23 patients from both the machine learning model and the CeTh metric. Values above 0 are classified as consciousness recovery (CR), while values below 0 are classified as non-recovery (unCR). The dashed line represents the model’s classification threshold. Vertical connecting lines show the difference between each patient’s decision values as determined by the model and the CeTh metric. Source data are provided as a Source Data file.

**CeTh features discriminate two subgroups of CR patients**

The reduced patient similarity within the CR group suggests the presence of more nuanced classes beyond the simple dichotomy of CR and unCR. Next, we examined this possibility using unsupervised hierarchical agglomerative clustering based on CeTh features to

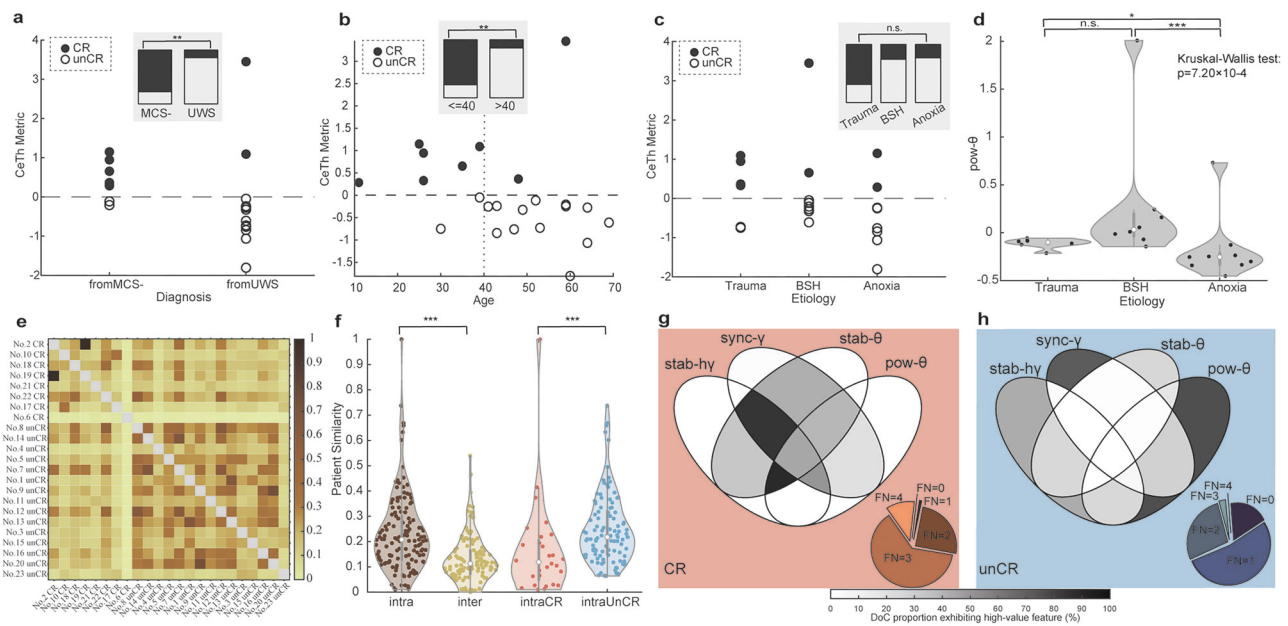


**Fig. 2 | CeTh neurophysiological features associated with DoC prognosis.** Distribution of central thalamus (CeTh) metric scores across various clinical factors: **a** clinical baselines (MCS-,  $n = 8$ ; UWS,  $n = 15$ ), **b** age (younger patients  $\leq 40$  years,  $n = 8$ ; older patients  $> 40$  years,  $n = 15$ ), and **c** etiologies (trauma,  $n = 6$ ; brainstem hemorrhage [BSH],  $n = 8$ ; anoxia,  $n = 9$ ). Each data point represents one independent patient. Solid circles represent CR patients and open circles represent unCR patients. The dotted line indicates the recovery threshold for the CeTh metric. Inset bar graphs depict the proportion of CR patients (solid) versus unCR patients (open) within each group. Statistical analysis of the inset was performed using two-sided Fisher's Exact Test: **a**  $p = 0.006$ , odds ratio = 16.10 (95% CI: 1.59–288.61), Cohen's  $h = 1.35$ ; **b**  $p = 0.006$ , odds ratio = 16.10 (95% CI: 1.59–288.61), Cohen's  $h = 1.35$ ; **c**  $p = 0.250$  (no significant difference among the three etiology groups). **d** The  $\text{pow-}\theta$  strength of the CeTh among etiologies ( $n = 6$  trauma,  $n = 8$  BSH,  $n = 9$  anoxia). Statistical analysis was performed using Kruskal–Wallis test (Conover's  $F = 10.618$ ,  $df = 2.20$ ,  $p = 7.20 \times 10^{-4}$ ,  $\eta^2 = 0.515$ ), followed by post-hoc Conover's All-Pairs Rank Comparison Test with no adjustment for multiple comparisons: trauma vs BSH  $p = 0.056$ , BSH vs anoxia  $p = 1.72 \times 10^{-4}$ , trauma vs anoxia  $p = 0.042$ . **e** CeTh-based patient-similarity matrix ( $N = 23$  patients: 8 CR, 15 unCR): The upper left region illustrates intra-CR patient similarity, and the lower right region shows intra-unCR patient similarity. **f** Statistical analysis of similarities from the patient-similarity matrix, including intra-group similarity, inter-group similarity, intra-CR similarity and intra-unCR similarity. Statistical comparisons were performed using two-sided Wilcoxon Rank Sum Test: intra-group vs inter-group similarity  $p = 1.98 \times 10^{-10}$ , intra-

CR vs intra-unCR similarity  $p = 1.18 \times 10^{-4}$ . Notably, these observed statistical differences in patient-similarity are only evident with the selected CeTh metric and do not show significant differences prior to feature selection (Supplementary Fig. 5). Violin plots in (**d**, **f**) show median (center white point), interquartile range (box bounds), and whiskers ( $1.5 \times$  interquartile range). **g** Venn diagram illustrates CeTh feature pattern in CR patients. The accompanying pie chart details the distribution of patients categorized by the number of features exhibiting high values simultaneously (high-value feature number, FN): only 0.93% exhibit high values in a single feature; 25.27%, 62.47%, and 11.33% in two, three, and four features (FN = 1, 2, 3, 4), respectively, with no patients exhibiting low values in any features (FN = 0). **h** Venn diagram and pie chart depict the CeTh feature pattern in unCR patients with a tendency of high values in only a single feature (FN = 1), predominantly  $\text{sync-}\gamma$  or  $\text{pow-}\theta$ . A majority of unCR patients (53.11%) show high values in just one feature, with 27.40% and 2.63% showing high values in two and three features (FN = 2, 3), respectively. None exhibit high values coherently across four features (FN = 4), and 16.85% with zero (i.e., showing low values in all features, FN = 0). Percentages in (**g**, **h**) are based on resampled data to address class imbalance (see “Venn diagram analysis of feature combinations” in “Methods”). UWS unresponsive wakefulness syndrome, MCS- minimally conscious state minus, CR consciousness recovery, unCR consciousness non-recovery,  $\text{stab-}\theta$  stability in the theta band,  $\text{stab-}\gamma$  stability in the high-gamma band, n.s. no significance for  $p \geq 0.05$ , \* for  $p < 0.05$ ; \*\* for  $p < 0.01$ ; \*\*\* for  $p < 0.001$ . Source data are provided as a Source Data file.

search for possible subgroups. As a result, we identified three subgroups (Fig. 3a and Supplementary Fig. 6a, b).

Subgroup I exhibited overall lower values across all four features (Fig. 3c and Supplementary Fig. 6c, d). Subgroup II featured higher  $\text{pow-}\theta$  and  $\text{sync-}\gamma$  (Fig. 3d and Supplementary Fig. 6c, d). Subgroup III was characterized by higher  $\text{stab-}\theta$  and  $\text{stab-}\gamma$  (Fig. 3e and Supplementary Fig. 6c, d). We found that none of the patients in Subgroup I exhibited recovery. That is, all CR patients were exclusively in subgroups II and III. Statistical tests confirmed that Subgroups II and III exhibited a higher recovery ratio than Subgroup I (Fisher's Exact Test,  $p = 0.005$  for three-group differences; Subgroup I vs. II,  $p = 0.011$ , Cohen's  $h = -1.68$ ; Subgroup I vs. III,  $p = 0.011$ , Cohen's  $h = -2.09$ ; no statistical difference between Subgroup II and III with  $p = 1.000$ ). Taken together, these results suggest that the CR group could be further divided into two classes, each with distinct CeTh features.

In addition, these three subgroups showed significant differences in their initial clinical baselines regarding UWS or MCS- (Fisher's Exact Test,  $p = 6.61 \times 10^{-4}$ ). Subgroup I consisted exclusively of UWS patients (Fig. 3b and Supplementary Fig. 6e). Subgroup II primarily consisted of

MCS- patients (7 out of 9) (Fig. 3b and Supplementary Fig. 6e). Subgroup III predominantly comprised UWS patients (3 out of 4) (Fig. 3b and Supplementary Fig. 6e). Interestingly, in our study, only two patients recovered consciousness from the UWS state, both of whom belonged to Subgroup III (Supplementary Table 1). Statistical analyses revealed no significant difference in age (Fisher's Exact Test,  $p = 0.105$ ) or etiology among three subgroups (Fisher's Exact Test,  $p = 0.820$ ). In summary, CeTh features differentiate two subgroups of patients who exhibit favorable recovery potential, with notable differences in their recovery modes. Subgroup II patients recovered exclusively from the MCS- state, whereas Subgroup III patients showed surprising recovery from the UWS state.

### Simulation of neural dynamics underlying theta rhythms in the CeTh of DoC patients

The features of theta rhythms in the CeTh, especially  $\text{stab-}\theta$  and  $\text{pow-}\theta$ , were identified as the most crucial contributors to the CeTh metric (Supplementary Table 4, see also Eq. 13 in “Methods”). These theta/alpha rhythms, indicative of the low-threshold bursting (LTB) regime

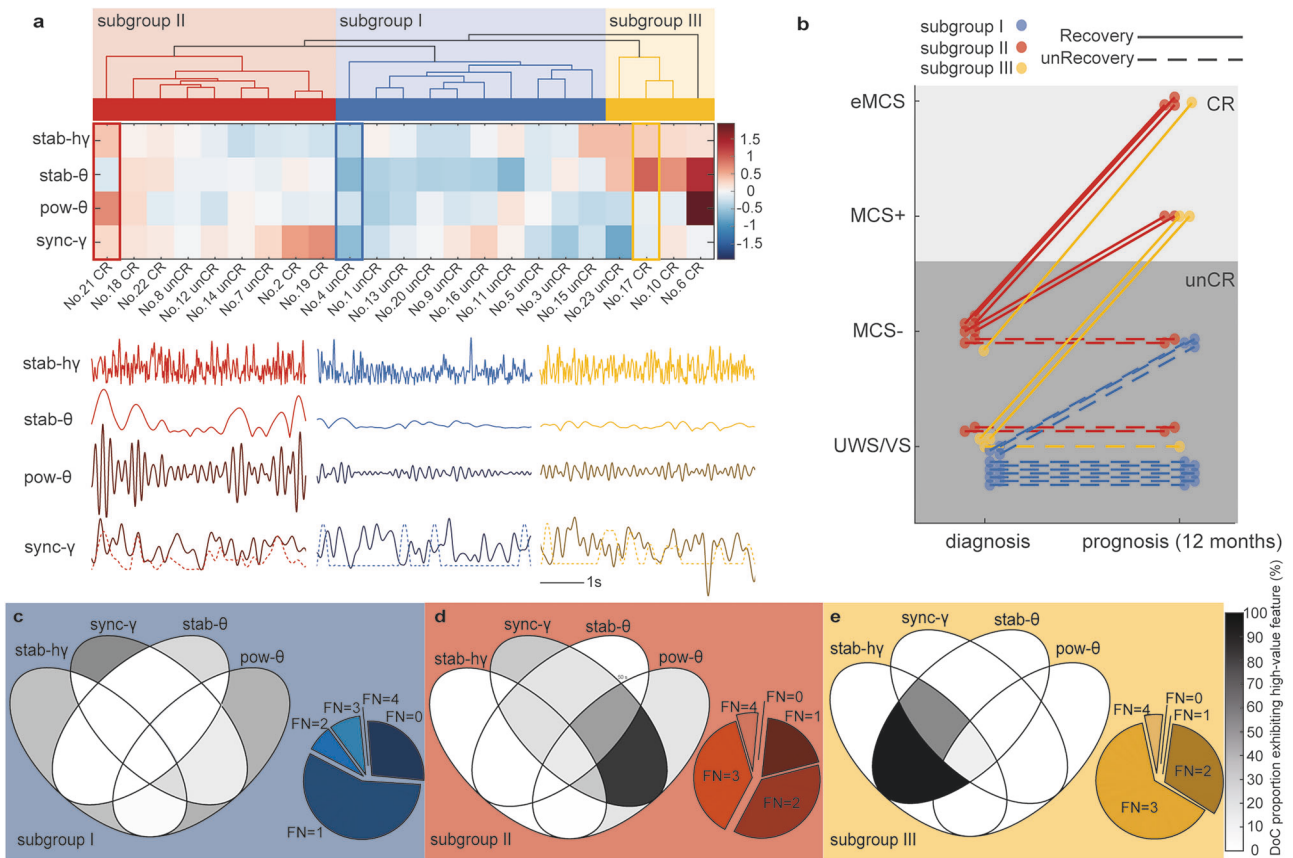


**Fig. 3 | CeTh-based subgrouping of DoC patients and their implications for consciousness states.** **a** Hierarchical agglomerative clustering of central thalamus (CeTh) features categorizes DoC patients into three subgroups (I, II, and III), with each column representing a patient and each row a CeTh feature. Visualization of four features in an example from each subgroup: Patient No. 21 (II), No. 4 (I), and No. 17 (III). Patient No. 21 (II) exhibits stronger theta band oscillation (pow- $\theta$ ) and increased synchronization between gamma band MUA fluctuations (solid line) and neuronal spiking (dotted line), indicating enhanced sync- $\gamma$ . Patient No. 17 (III) shows both higher stab- $\theta$  and stab-hy, illustrated by the stability of the displayed envelopes corresponding to oscillations. Conversely, Patient No. 4 (I) exhibits weaker theta rhythms (pow- $\theta$ ), reduced and even negative sync- $\gamma$ , and more pronounced instability in the envelopes of oscillations (stab- $\theta$  and stab-hy). **b** Changes in consciousness states pre- and post-CeTh-DBS therapy across 23 patients. Solid lines indicate patients who improved to CR after treatment, while dashed lines represent those who remained unCR. All CR patients exhibited significant improvements after 12 months CeTh-DBS treatment. **c–e** Venn diagrams and accompanying pie charts depict CeTh feature profiles in each subgroup. Subgroup I mainly shows low feature

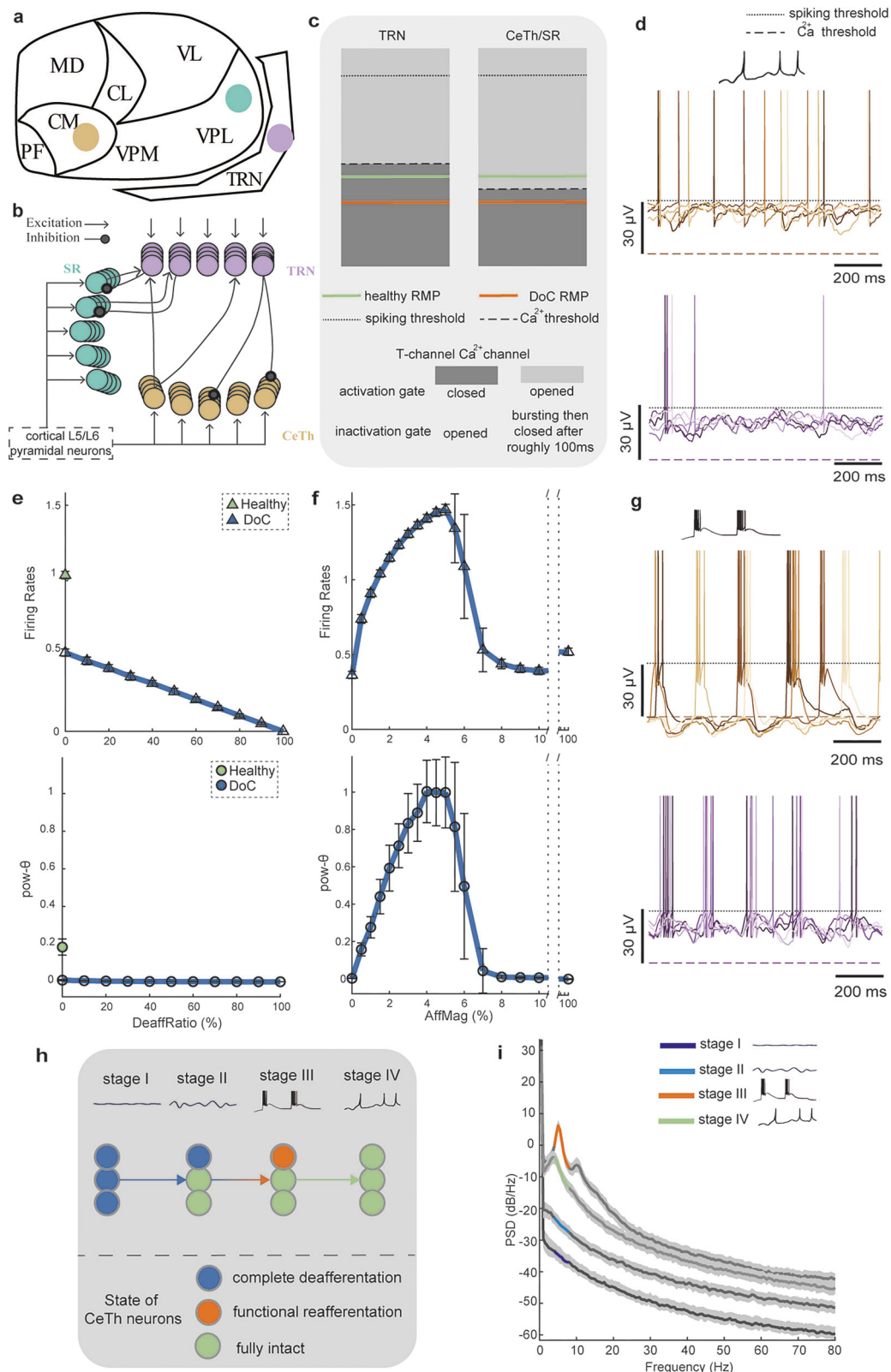
values (**c**). Subgroup II predominantly exhibits high values in pow- $\theta$  and sync- $\gamma$  (**d**), while Subgroup III is characterized by high values in stab- $\theta$  and stab-hy (**e**). Pie charts show patient distribution by number of concurrent high-value features (FN): Subgroup I—57.07% with one feature, 6.68% with two, 8.86% with three, 0% with four features (FN = 1, 2, 3, 4) and 27.39% with zero (FN = 0) (inset in **c**). Subgroup II—18.99% with one, 37.90% with two, 36.77% with three, 6.24% with four, and 0.10% with zero (FN = 1, 2, 3, 4, 0, inset in **d**). Subgroup III—0% with one, 31.43% with two, 64.21% with three, 4.36% with four, and 0% with zero (FN = 1, 2, 3, 4, 0, inset in **e**). Percentages in (**c–e**) are based on resampled data to address class imbalance (see “Venn diagram analysis of feature combinations” in “Methods”). CR consciousness recovery, unCR consciousness non-recovery, UWS unresponsive wakefulness syndrome, MCS- minimally conscious state minus, MCS+ minimally conscious state plus, eMCS emergence from minimally conscious state, stab- $\theta$  stability in theta band, pow- $\theta$  theta band power, sync- $\gamma$  spiking-MUA synchronization in the gamma band, stab-hy, stability in the high-gamma band. Source data are provided as a Source Data file.

mediated by T-type calcium channels, are well-established neurophysiological characteristics<sup>49–52</sup> in the thalamus during altered consciousness under anesthesia and sleep<sup>47–49,53</sup>. Our finding of the significance of theta rhythms suggested a similar LTB regime in DoC (Fig. 1b). To examine this issue, we developed a biophysical model for CeTh activity that incorporates DoC-specific physiological conditions and investigated whether it can generate theta rhythms. The model included three thalamic nuclei—thalamic reticular nucleus (TRN), CeTh, and specific relay nuclei (SR) (Fig. 4a,b)—crucial for modulating awareness/arousal<sup>22,23,30,48,53–56</sup>. Under normal conditions of both membrane potential and afferent inputs<sup>57</sup> (Fig. 4c), the model exhibited desynchronized tonic firing activity, similar to that observed during healthy wakefulness in the thalamus<sup>9,58,59</sup> (Fig. 4d).

The pathophysiological mechanism underlying DoC involves the reduction of excitatory synaptic activity, attributed to structural/functional deafferentation and a lowered neuronal resting membrane potential (RMP)<sup>9,47,58,59</sup>. Thus, we simulated CeTh activity under lower

RMPs (Fig. 4c) and various afferent conditions. We found that merely increasing the proportion of deafferented neurons (deaffRatio) induced a quiescent state with marginally reduced firing rates, but did not introduce theta rhythms in the CeTh (Fig. 4e). However, additionally augmenting the magnitude of residual afferent input (affMag) in those affected neurons shifted neuronal activity toward an LTB regime (Fig. 4g), facilitating the emergence of theta rhythms, accompanied by a similar change in firing rates (Fig. 4f). These results reveal how the theta rhythmic state is generated in the CeTh of DoC patients.

To further simulate the CeTh state in different stages of DoC recovery, we varied RMPs, deaffRatio, and affMag in the model. Stage I features deafferentation in more than 90% of neurons in the CeTh; Stage II involves deafferentation in 30% of CeTh neurons; Stage III represents a theta rhythmic intermediate state; and Stage IV marks full recovery to a healthy profile (Fig. 4h, see “Methods”). During the transition from Stage III to IV, our simulations revealed that both full reafferentation and restoration of membrane potential are necessary



for the CeTh to finally return to a tonic regime (Fig. 4e,f). Conversely, for the transition from Stage II to I, the decline in neurological condition resulted from increasing deaffRatio and led to a further reduction in CeTh firing rates (Fig. 4e). Collectively, these findings across four stages are consistent with the distinct CeTh dynamics as outlined in the “ABCD” model<sup>58,59</sup>, which is a theoretical framework that describes CeTh activity patterns under varying levels of consciousness.

Additionally, these findings reveal a biphasic pattern of theta rhythms in the simulated CeTh neurons, characterized by an initial emergence (I to III) followed by a decline (III to IV) during functional recovery (Fig. 4f, i). This biphasic pattern mirrors a similar, biphasic pattern of theta/alpha rhythm during anesthesia<sup>47,60</sup>, indicating a potential shared mechanism underlying different levels of consciousness during loss of consciousness (LOC) under DoC and anesthesia.

**Fig. 4 | Network simulation of neural dynamics underlying theta rhythms in CeTh.** **a** Schematic of thalamic nuclei (coronal view): central thalamus (CeTh), thalamic reticular nucleus (TRN), and the specific relay nucleus (SR). The SR encompasses first-order sensory relay nuclei such as the ventral posterior nucleus (somatosensory), the medial geniculate nucleus (auditory), and the lateral geniculate nucleus (visual). **b** Network connectivity diagram illustrating that the SR is wired to the TRN with one-to-one connections, and the CeTh is linked to the TRN with random one-to-many connections (see Supplementary Table 5). **c** Diagram of thalamic neuronal parameters, including the healthy and DoC resting membrane potential (RMP, solid line), spiking threshold (dotted line), and the threshold for T-type calcium channels (dashed line, see Supplementary Table 6). Specifically, when the membrane potential is initially below the calcium threshold, the calcium inactivation gate remains open. Once the potential exceeds this threshold, the calcium activation gate also opens, leading to a low-threshold bursting (LTB) regime for roughly 100 ms before the inactivation gate closes<sup>104</sup>. **d** Tonic regime traces from five example CeTh neurons and five TRN neurons, with raster plots in the Supplementary Fig. 7a. **e** State transitions under complete deafferentation (no

residual input for affected neurons) are demonstrated by varying proportions of deafferented neurons (deaffRatio), and measured through changes in firing rates and theta band power (pow- $\theta$ ). The healthy profile is also depicted, characterized by a deaffRatio of 0% and the restoration of normal RMP. **f** State transitions under reafferentation with various magnitudes of residual afferent inputs (affMag). The firing rate and pow- $\theta$  are shown during the transition from complete deafferentation to a theta rhythmic state, and then to further reafferentation. The deaffRatio is set at 30%, a level that would not significantly affect rhythmic properties, as shown in **(e)**. Data in **(e, f)** are presented as mean values  $\pm$  standard deviation ( $N=100$  independent simulation runs). **g** Bursting regime traces from five CeTh neurons and five TRN neurons, with raster plots in Supplementary Fig. 7b. **h** Diagram illustrating the CeTh status across four stages (see “Methods”). **i** Power spectral density (PSD) of CeTh across four stages, with theta band power highlighted. Data are presented as mean values ( $N=100$  runs), with shaded regions representing standard deviation around the mean PSD values. Source data are provided as a Source Data file.

### Neural dynamics underlying different recovery modes of DoC

As demonstrated above, two subgroups with favorable recovery after CeTh-DBS displayed distinct CeTh theta rhythm profiles, characterized by higher pow- $\theta$  (II) and stab- $\theta$  (III), respectively (Fig. 3d, e). This variation suggested that pow- $\theta$  and stab- $\theta$  are largely independent parameters of the theta rhythm for measuring different CeTh states in DoC. Additionally, studies have shown that neuronal activities become increasingly unstable in the thalamocortical circuit as the level of consciousness diminishes during LOC under deep anesthesia. These unstable activities were driven by slow oscillations and/or burst suppression, either of which significantly altered the membrane potential<sup>47,48,61,62</sup>. Thus, to closely examine the effects of both power and stability of the theta rhythm, we simulated the CeTh state transition from the quiescent state (Stage II) to the theta rhythmic state (Stage III). Specifically, we varied both affMag and the stability of afferent inputs (affStab) to CeTh neurons (Fig. 5a).

We found that increasing affMag monotonously enhanced pow- $\theta$  while minimally affecting stab- $\theta$  (Fig. 5b, e). Similarly, affStab increased stab- $\theta$  without significantly affecting pow- $\theta$  (Fig. 5c, d). As a result, increases in affMag and affStab, respectively, enhanced the power and the stability of theta band activities. The changes in firing rates were in line with those of pow- $\theta$  during these processes (Supplementary Fig. 8). Furthermore, two neurodynamic modes could be identified (Fig. 5f, g). Mode A involves increasing the affMag first, followed by affStab, leading to an enhancement in the pow- $\theta$  first, followed by stab- $\theta$ . Conversely, Mode B follows the opposite sequence, increasing stab- $\theta$  first and subsequently pow- $\theta$ . These two neurodynamic recovery modes respectively correspond to the empirical data observed in Subgroups II and III (Supplementary Fig. 9), suggesting that they may underpin the distinct CeTh profiles discovered in these two recoverable subgroups (Supplementary Fig. 10).

### Discussion

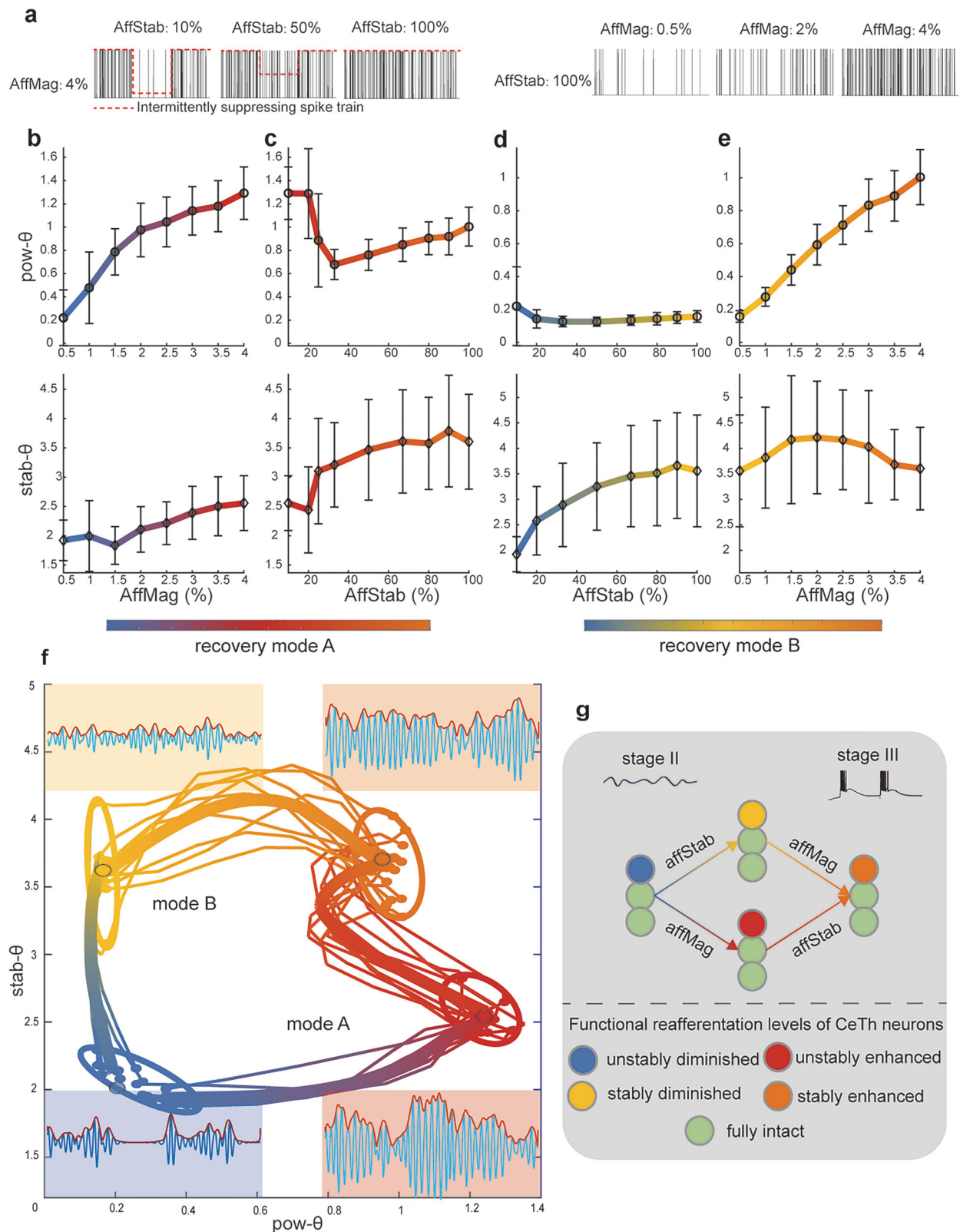
The CeTh's well-established role as a bi-directional hub in arousal regulation<sup>22–30</sup> underscores its importance in exploring neural mechanisms underlying DoC. Our results confirm that CeTh status consistently serves as an indicator of functional recovery after CeTh-DBS in patients with prolonged altered awareness across diverse clinical factors, despite considerable heterogeneity, including highly varied etiologies, clinical baselines, and ages. Notably, based on CeTh activities, we identified two distinct subgroups (II and III) of patients with different clinical baselines yet similarly favorable outcomes. Biophysical modeling demonstrated two neurodynamic pathways underlying the CeTh's theta rhythmic state, each corresponding to a subgroup we observed empirically.

We found that etiological differences are primarily indicated by the pow- $\theta$  in the CeTh. This can be understood in light of our

simulation results, which show that pow- $\theta$  is affected by the damage to the CeTh neurons per se (simulated as complete deafferentation in the model) and by the magnitude of neuronal afferent input to the CeTh. Anoxic patients primarily experience thalamo-cortical gray matter damage<sup>63</sup>. According to our simulations, damage to CeTh neurons per se led to diminished theta rhythms. Indeed, this group of patients exhibited the lowest pow- $\theta$  in our empirical results. In contrast, traumatic patients mainly experience thalamo-cortical white matter damage with diffuse axonal injury, leading to less degrees of deafferentation to CeTh<sup>64</sup>. Compared to complete deafferentation, these patients may preserve certain residual neuronal inputs and thus exhibit higher pow- $\theta$  than those in anoxia, as demonstrated by our simulations and corroborated by the patients' data. Meanwhile, patients with BSH, retaining considerable thalamo-cortical integrity, could result in highly preserved residual afferent input to CeTh neurons and, consequently, the highest pow- $\theta$  among all etiologies. Taken together, these results suggest that a shared CeTh mechanism underlies the varying electrophysiological manifestations seen in different causes of brain damage that lead to DoC. This implies that DoC is not simply an umbrella term for separate pathologies with overlapping symptoms of impaired consciousness, despite the heterogeneous underlying causes.

Moreover, we identified two distinct subgroups (II and III) of patients with recovery potential. Subgroup II, characterized by high pow- $\theta$ , likely retains a high magnitude of afferent neuronal input within neurodynamic Mode A. Subgroup II also exhibits better clinical baselines. Thus, neurodynamic mode A may underpin the pathophysiological mechanisms behind the higher recovery probabilities observed in individuals with better diagnoses<sup>3,12</sup>. Conversely, Subgroup III, characterized by high stab- $\theta$ , likely preserves highly stable afferent neuronal input within neurodynamic Mode B. Despite poor clinical baselines, Subgroup III demonstrated a favorable prognosis. Therefore, neurodynamic mode B may serve as the neurophysiological basis for another subgroup showing recovery potential, albeit with poor baselines and fewer in number<sup>3,11,12</sup>. Similar manifestations—poor baselines yet potential for recovery—have been previously identified in cases of covert consciousness or cognitive motor dissociation<sup>9,65–69</sup>. However, the relationship between our findings and these conditions remains unclear, necessitating further investigation. This divergence indicates that early clinical assessments cannot capture the neurodynamic complexity or accurately estimate the recovery potential for certain patients, which aligns with the suggestion that more information should be taken into account<sup>69–71</sup>.

During altered consciousness induced by sleep and anesthesia, slow oscillations accompany overall membrane potential fluctuations, resulting in alternating ON-OFF periods and interrupting stable theta/alpha rhythms<sup>47,61,62</sup>. As anesthesia deepens, enhanced synaptic



inhibition leads neural networks to further transition towards an isoelectric state<sup>40,72,73</sup>. During this transition, burst suppression—a marker of deep anesthesia—intermittently mutes oscillations, leading to an increasingly unstable activity pattern<sup>47,74</sup>. The theta rhythm mentioned above is sustained by stable excitatory-inhibitory interactions between the central thalamus and the inhibitory TRN<sup>48,49,52,53</sup>. Enhanced inhibition provided by the TRN to CeTh cells prompts the latter to generate

LTBs via T-type low-threshold calcium channels. The TRN cells, in turn, respond to these bursts from CeTh, thus promoting a thalamic inhibitory-excitatory rhythm. Similarly, during LOC under absence seizures, corticothalamic contribution enhances thalamic theta oscillations through modulating thalamic relay-TRN interactions<sup>75</sup>. However, this theta rhythm is absent when the brain remains in a quiescent isoelectric state, as observed during LOC under very deep anesthesia,

**Fig. 5 | Two modes of neural dynamics underlying DoC recovery.** **a** Illustration of residual input to central thalamus (CeTh) neurons. Left: Input stability manipulation through “OFF periods”, with afferent stability (affStab) ranging from 10 (90% of spikes muted during “OFF periods”) to 100% (no suppression) while afferent magnitude (affMag) remains constant. Right: three examples of Poisson spike trains with varying discharge probabilities. AffMag ranges from 0.5 to 4%, with affStab consistently at 100%. **b–e** State transitions from a quiescent state (Stage II) to a rhythmic state (Stage III), illustrating the effects of varied afferent conditions on CeTh neurons. Data are presented as mean values  $\pm$  standard deviation ( $N = 100$  independent simulation runs). “Varied afferent conditions” encompass variations in both magnitude (affMag) and stability (affStab) of residual inputs to CeTh. **b, e** Assess transitions under varied affMag, while **c, d** focus on transitions under

varied affStab. For each subplot, the top panels display theta band power ( $\text{pow-}\theta$ ) of the CeTh and the bottom panels show the stability in the theta band ( $\text{stab-}\theta$ ). Recovery Mode A corresponds to **(b, c)** and Recovery Mode B corresponds to **(d, e)**. **f** Depiction of two recovery modes of CeTh neural dynamics in the feature space of the theta rhythm. Fine lines represent average trajectories from ten simulation runs each, and the thick line indicates the overall average across all simulation runs ( $N = 100$ ). Four circled areas denote distinct states of CeTh corresponding to different combinations of  $\text{stab-}\theta$  and  $\text{pow-}\theta$  levels (low/high), as indicated by their positions in the feature space. Insets show theta rhythm profiles from four simulated CeTh examples at each corner. **g** Diagram illustrating two recovery modes as CeTh transitions from Stage II to Stage III. Five afferent conditions affecting the CeTh are considered. Source data are provided as a Source Data file.

resulting from a highly hyperpolarized membrane potential<sup>72,73</sup>. In our empirical results, the  $\text{pow-}\theta$  and the  $\text{stab-}\theta$  in the CeTh of DoC patients distinctly capture their status, ranging from quiescence to a theta rhythmic state. Dynamical simulations demonstrate that this theta rhythmic state is caused by LTB in the CeTh. Taken together, these results strongly suggest that the mechanism underlying LOC in DoC parallel those observed during anesthesia. By linking DoC to well-established LOC mechanisms, our findings pave the way towards a thorough understanding of DoC and its recovery processes.

While our recordings were obtained from a single nucleus, the CeTh's unique anatomical and functional properties allow it to serve as a window into broader network states. Anatomically, CeTh's position as a bidirectional hub enables it to integrate and reflect the loss of inputs following multi-focal brain injuries<sup>9,76</sup>. Functionally, the electrophysiological features we identified, particularly theta rhythms, emerge from network-level interactions involving multiple thalamic nuclei and cerebral cortical inputs. To achieve the high-resolution assessment necessary for understanding this critical hub's role in DoC, invasive CeTh recordings were analyzed in this study. While CeTh provides valuable prognostic information for DoC, we acknowledge that other cerebral regions also play important roles in consciousness<sup>18–21,77–79</sup>.

It is important to recognize that all patients in this study underwent CeTh-DBS treatment, so the prognostic features identified should be interpreted as markers that signal recovery potential in response to DBS. This intervention has been associated with improved recovery rates in DoC patients<sup>11–14</sup> and has also demonstrated efficacy in awakening non-human primates from anesthesia<sup>26–28</sup> and in treating patients with moderate-to-severe traumatic brain injury<sup>80</sup>. Spontaneous recovery in DoC patients is rare due to the lack of effective treatments<sup>13</sup>, which means some patients who remain unconscious may have severe, irreversible damage, but others may still retain recovery potential that goes unrecognized without active neuromodulation. Since the present study did not include a matched control group, the extent to which the observed effects can be attributed to DBS remains uncertain. Future studies that incorporate controlled experimental designs could help establish the broader prognostic value of the CeTh metric and delineate the role of DBS in promoting recovery. Given the close projection relationship between the thalamus and cortex<sup>16,26,27,30,81–83</sup>, the identification of features of theta rhythm in the CeTh in this study could guide the search for non-invasive prognostic markers. This study focuses exclusively on invasive CeTh recordings without concurrent EEG analysis, which represents a limitation in assessing broader cortical network dynamics<sup>19–21</sup>. In future studies, we aim to incorporate non-invasive EEG to identify external correlates of CeTh activity, while also conducting comparative observations across patients receiving different treatments, with the goal of translating these findings into a broader understanding of DoC that is applicable across treatment modalities and patient populations<sup>84</sup>.

The limited sample size is a major limitation of this study. To mitigate the impact of the small sample size, we (1) implemented a simple, interpretable linear SVM model with fewer hyperparameters,

thereby reducing model complexity and tuning requirements; and (2) used permutation tests based on shuffled datasets. The mean accuracy of ~50% on shuffled data was near the chance level of binary classification, indicating that our model did not overfit to “noise” in small samples. However, these cannot fully address the constraints imposed by the small sample size. For example, in the etiology analysis (Fig. 2d), further dividing the sample into small subgroups for each etiology led to insufficient statistical power. This may explain why the observed differences in CeTh between etiologies showed trends but did not reach statistical significance (e.g., trauma patients tended to have higher CeTh metric values, but the differences across etiologies were not statistically significant). Multi-center, independent cohort validation is necessary to confirm the generalizability of our findings and their translational value. Specifically, we found a link between thalamic theta rhythms and consciousness recovery. Validation of this finding in future studies may lead to useful clinical biomarkers and guide individualized intervention strategies for DoC patients.

## Methods

### Participants and surgical indications

To explore which patients are more likely to respond to CeTh-DBS and to gain deeper insight into the role of the central thalamus in consciousness recovery, we retrospectively analyzed intraoperative microelectrode recordings from patients with disorders of consciousness (DoC) who underwent CeTh-DBS. Among the consecutive 421 prolonged DoC patients admitted to our centers (Seventh Medical Center of PLA General Hospital and Beijing Tiantan Hospital) from June 2011 to June 2021, 39 DoC patients received CeTh-DBS treatment and were included in the study.

The eligibility criteria for DBS surgery included (1) absence of extensive skull defects, no prior skull repair or shunt pump implantation, (2) no significant surgical contraindications, and (3) an intact bilateral thalamus structure. A series of assessments were performed prior to surgery to evaluate the potential of regaining consciousness. These included a thorough medical history review, repeated clinical assessment, MRI, functional MRI, EEG, and Mismatch Negativity. Experienced clinicians assessed CRS-R scores through repeated evaluations at least three times. All patient evaluations were performed by the same clinical team following consistent diagnostic and treatment protocols across both centers. Patients who exhibited significant improvement in consciousness level (indicating a phase of spontaneous recovery) or significant deterioration (which may indicate other clinical complications unsuitable for surgery) within the previous four weeks, or patients with other neurological diseases or life-threatening systemic diseases were no longer considered for this intervention. Additionally, patients diagnosed with UWS and did not exhibit favorable prognostic indicators on any neurofunctional assessment were not further recommended for CeTh-DBS. Favorable indicators were considered qualitatively rather than by strict cutoffs—for example, preserved thalamocortical integrity and organized network activity on MRI/fMRI, normal or near-normal EEG background rhythms with features such as spindles, and discernible MMN responses. These findings

were interpreted by experienced clinicians and integrated into clinical judgment. All examination findings, uncertain clinical benefits and potential risks of the DBS procedure were fully discussed with the patients' legal guardians, who made the final decision to proceed with the surgery. It should be noted that this procedure was not part of a formal prospective clinical trial of efficacy, but rather an exploratory intervention conducted on a clinical/compassionate-use basis for individuals with prolonged DoC who lacked other effective treatment options.

Among the 39 DoC patients received CeTh-DBS, 11 patients without intraoperative microelectrode recordings were excluded. We further excluded two patients due to inaccurate electrode placement, two due to loss to follow-up, and one who died within three months from unrelated causes. Ultimately, 23 DoC patients' (15 UWS and 8 MCS-, 9 females and 14 males) data were analyzed in this study (Supplementary Fig. 11). Clinical information and MRI details for each patient are provided in Supplementary Table 1 and Supplementary Fig. 1. Following the principles of the Declaration of Helsinki, written consents were obtained from patients' legal guardians or next of kin, and the study received approval from the ethics committees of PLA Army General Hospital (protocol No: 2011-0415) and Beijing Tiantan Hospital, Capital Medical University (protocol No: 2017-361-01).

### Surgical and recording procedures

We targeted the bilateral CM-pf nuclei in the central thalamus, implanting multi-channel microelectrodes (Leadpoint, Medtronic, USA) for intraoperative electrophysiological recording. Data were extracted from the signal within a 1 mm range above and below the target. All procedures were performed under general anesthesia. To avoid potential influences on neuronal firing, the administration of propofol and sevoflurane was discontinued 20 min before microelectrode recordings. The microelectrode recordings were used to assist in accurately identifying the target nuclei. Recordings typically began ~10 mm above the intended CM-pf target and advanced in 0.5 mm steps. The trajectory often traversed the ventrolateral nucleus, characterized by higher firing rates and bursts, before reaching the CM-pf, where activity was relatively lower. Electrophysiological transitions were noted as the firing rate increased on entering the ventrolateral nucleus and decreased when advancing into the CM-pf. To refine depth, the electrode was advanced 1–2 mm beyond the target; if neuronal activity increased again, the lead was retracted to just above this point, ensuring the distal/deepest contacts were placed within the CM-pf. Once the optimal target location was confirmed, the microelectrodes were withdrawn, and quadripolar DBS leads (PINS L302, Beijing PINS) were subsequently implanted at the verified sites (Fig. 1a). Final lead positions were confirmed by postoperative CT or MRI.

### DBS treatment and prognosis evaluation

The implantable pulse generators (IPGs) were activated one week after surgery, following confirmation of wound healing and resolution of local edema around the implantation site. All patients included in this study received continuous DBS therapy throughout the follow-up period. Each day, stimulation was administered between 08:00 and 20:00 in a cyclic pattern of 15 min on and 15 min off. Stimulation parameters included a frequency of 100 Hz, a pulse width of 120  $\mu$ s, and a voltage ranging from 1.0 to 4.0 V.

Follow-up assessments were scheduled at 3, 6, and 12 months after DBS surgery. The Glasgow Outcome Scale and CRS-R were performed during each follow-up to assess the recovery and level of consciousness. After the one-year follow-up period was completed, the follow-up diagnoses were determined based on the best CRS-R score attained within this period. Before the analysis of prognosis features, patients finally diagnosed as UWS and MCS- were grouped as "consciousness non-recovery" (unCR), indicating a sustained absence of language processing evidence (command-following, intelligible verbalization,

and intentional communication)<sup>5–7</sup>. Conversely, patients who recovered to MCS+ and emergence from MCS (eMCS) were categorized as "consciousness recovery" (CR), showing marked improvement after CeTh-DBS treatment in regaining the ability to understand language or restore communications<sup>5–7</sup>. Based on the CRS-R scale, CR (MCS+ and eMCS) was operationally defined as achieving at least one of the following CRS-R subscale scores: auditory function  $\geq 3$  (reproducible/consistent movement to command), motor function  $\geq 6$  (functional object use), oromotor/verbal function  $\geq 3$  (intelligible verbalization), or communication  $\geq 1$  (intentional/accurate communication).

### Signal processing and feature extraction

The signal from each electrode was first amplified (10 $\times$ ), bandpass filtered (500–10,000 Hz), and sampled at 24 kHz (Alpha-Map 5.4; Alpha-Omega) online. For offline preprocessing, we first applied a bandpass filter between 500 and 5 kHz using third-order IIR filters (implemented with "designfilt" function using "highpassiir" and "lowpassiir" to create separate high-pass and low-pass filters, applied with "filtfilt" functions in MATLAB). We then applied notch filters to suppress 50 Hz power-line interference and its harmonics using eighth-order Butterworth bandstopiir filters (implemented with "designfilt" with "DesignMethod" set to "butter" and applied with "filtfilt" functions in MATLAB). Signal segments containing large artifacts were manually detected and excluded. The preprocessed signal was then extracted into two distinct modalities: neuronal spikes and Multiunit Activity (MUA), as depicted in Fig. 1b.

Multiple spikes (MSPs) were identified when peak or valley amplitudes exceeded 5 times the estimated background noise level<sup>85</sup>, followed by waveform shape validation<sup>86</sup>. The background noise level was estimated using a signal envelope approach. Specifically, the signal envelope (which follows the Rayleigh distribution for band-limited signals) was computed using the Hilbert transform ("hilbert" function in MATLAB), and the noise level was determined as the mode of the envelope amplitude distribution (through "histogram" function). This envelope-based approach is robust to the presence of high-frequency spiking activity and artifacts<sup>85</sup>. Although single-unit isolation using the Offline Sorter (Plexon) was attempted, reliable single-unit clustering could not be achieved for many DoC patients, consistent with previous reports of "notably silent" central thalamic activity<sup>31</sup>. Thus, we adopted MSPs for subsequent analyses as the MSP approach provided consistent neuronal firing measures for each patient without data exclusion<sup>36,86</sup>.

The MUA calculation followed the previous study<sup>36,87,88</sup>. Specifically, we first clipped extreme values by truncating values exceeding the mean by more than  $\pm 2$  standard deviations (SDs). The root mean square (RMS) was then calculated: firstly, squaring the values to provide an instantaneous measure of spike-band power; secondly, applying a low-pass filter using a third-order Butterworth filter at 100 Hz ("butter" and applied with "filtfilt" functions in MATLAB), then reducing the sampling rate to 500 Hz using the "downsample" function; and finally, taking the square root to obtain the preliminary MUA. Final MUA was obtained after outlier removal using moving average RMS (implemented with 20 ms sliding window and "rms" function with threshold of 2.58 SDs in MATLAB).

Next, we analyzed 34 electrophysiological features of the CeTh (Fig. 1c, left), categorized into five primary properties:

**Neuronal firing properties.** Including neuronal firing rates and firing activity patterns. The firing rates were calculated using a 1s-long sliding window with 50% overlap, providing a sampling rate of 1 Hz for the binned multiple spike firing rates. The degree to which spikes are temporally aggregated was assessed through two metrics. The first metric is the spike-clustering index, which is defined as the ratio between the number of inter-spike intervals (ISIs) less than 20 ms and those of 20 ms or greater. The second metric is the spike-clustering ratio, which compares the total duration of clustered spikes (ISI < 20 ms)

to the duration of non-clustered spikes ( $ISI \geq 20$  ms). Similarly, the degree to which spiking activities are suppressed intermittently was quantified using the pause index and the pause ratio. The pause index is the ratio between the number of ISIs of 100 ms or greater and those shorter than 100 ms, and the pause ratio measures the total duration of pauses ( $ISI \geq 100$  ms) against the duration without pauses ( $ISI < 100$  ms)<sup>89</sup>.

**MUA properties.** Comprising the mean value of MUA (MUAm<sub>mean</sub>) and both the raw and normalized power (represented as percentage of the total power across 0.5–250 Hz) across six frequency bands. The frequency band includes delta (0.5–4 Hz), theta (4–8 Hz), alpha (8–14 Hz), beta (14–30 Hz), gamma (30–50 Hz), and high-gamma (50–80 Hz). These features are denoted as MUApower(raw)Theta, MUApowerTheta (abbreviated as pow- $\theta$ ), etc. The power strength was estimated using Welch's method ("*pwelch*" function in MATLAB) with a Hamming window of 50% overlap, and a frequency resolution of 0.5 Hz.

**Signal stability.** Covering firing rate stability (FiringRatesstability), overall MUA stability (MUAstabilityBroadband), and band-specific stability (e.g., MUAstabilityTheta, MUAstabilityHGamma, abbreviated as stab- $\theta$  and stab-h $\gamma$ , respectively). The signal envelopes are determined first using the Hilbert transformation ("*hilbert*" function in MATLAB). For frequency-specific stability analysis, signals were first filtered into respective frequency bands using fourth-order Butterworth filters ("*butter*" and applied with "*filtfilt*" functions in MATLAB) before envelope extraction. A one-second sliding window then assesses local standard deviation trends over time using the "*movstd*" function. Finally, the coefficient of variation (CV) quantifies the relative standard deviation to the mean ( $CV = \text{std}/\text{mean}$ ), and the inverse of the CV serves as the stability strength indicator.

**Spiking-MUA synchronization.** Referring to the synchronization between neuronal firing rates and MUA activity (syncMUA). Pearson correlations (using "*corr*" function in MATLAB) were calculated between neuronal firing rates and MUA spectral power using 0.2s-long sliding windows with 50% overlap for both signals. The time-frequency representation of MUA was obtained using the "*spectrogram*" function in MATLAB. Correlations were computed for broadband power spanning 0.5–250 Hz (syncMUABroadband) and for specific frequency bands (e.g., syncMUAGamma, abbreviated as sync- $\gamma$ ).

The features based on MUA include MUA raw power, MUA normalized power, MUA stability, and spiking-MUA synchronization. An additional spikelessing step (spike removal procedure) on MUA was performed for these features except for the spiking-MUA synchronization. For each raw record, the spikelessing step involved subtracting the average spike waveform template from all the detected spike locations before the MUA estimation<sup>36</sup>.

**Background noise level.** As described in the spike detection section, background noise levels were extracted using the signal envelope approach with the mode of the envelope amplitude distribution<sup>44</sup>.

Data from multiple trials were collected for each subject. For each electrophysiological feature, the median value across all trials was calculated to obtain a single representative measure per patient to reduce variability. Furthermore, all these features were normalized at the subject level using Z-score normalization before the feature selection<sup>33</sup>.

### Feature selection

To identify the optimal CeTh feature combination for individual prognosis, we utilized a machine-learning pipeline composed of five steps (Supplementary Fig. 2a).

**Step 1 clustering features.** Given the redundancy observed among the original 34 CeTh features (Fig. 1c, left), we performed hierarchical

agglomerative clustering. The clustering was performed using an agglomerative approach with the "*linkage*" function in MATLAB. We applied the Weighted Pair Group Method with Arithmetic Mean (WPGMA) as the *linkage* method, which uses a recursive definition to calculate the distance between two clusters as follows:

$$d(r, s) = \frac{d(p, s) + d(q, s)}{2} \quad (1)$$

where  $r = p \cup q$  represents the newly formed cluster from clusters  $p$  and  $q$ , and  $s$  is another cluster.

The pairwise distances between CeTh features were calculated using Spearman correlation, specified by setting the "*METRIC*" parameter to "*spearman*" and the "*METHOD*" parameter to "*weighted*" in the "*linkage*" function. This bottom-up approach initially treats each data point as an individual cluster, then progressively merges the closest clusters according to the defined distance metric. The clustering process was terminated by setting a threshold on the intra-cluster correlation strength. Specifically, we set the threshold to ensure all pairs of features within each cluster maintained a Spearman correlation strength with  $|r| \geq 0.8$ , representing very strong correlations<sup>90</sup>. This yielded 21 clusters, with intra-cluster correlations in all multi-feature clusters exceeding the threshold (minimum observed  $|r| = 0.824$ ). The hierarchical cluster tree generated from the "*linkage*" function was visualized using the "*dendrogram*" function in MATLAB as depicted in Supplementary Fig. 2d. Using the cluster assignments obtained from the "*dendrogram*" function, we identified the members of each cluster, as listed in Supplementary Table 2. For each cluster, we computed the arithmetic mean of all features within that cluster, creating a single representative feature per cluster. These cluster-center features were used for subsequent analyses to reduce redundancy and displayed in Supplementary Fig. 2e.

**Step 2 filtered feature selection.** The filtered feature selection approach assigns relevance scores to each feature based on predefined metrics, selecting only those exceeding a specified threshold. This method is computationally efficient and suitable for high-dimensional data. Moreover, as it is independent of any machine learning algorithms, filter methods avoid classifier bias<sup>91,92</sup>. For 21 cluster-center features, we applied three filtering criteria: (1) statistical significance ( $p < 0.05$ ), (2) medium to large effect sizes ( $|r| > 0.3$ )<sup>93</sup>, and (3) Fisher Scores above the inflection point<sup>94</sup> (as shown in the Supplementary Fig. 2b). These three criteria generated three distinct filtered feature subsets that were then used in Step 3.

Statistical significance was evaluated using the Wilcoxon Rank Sum Test (two-tailed, unpaired) to identify significant differences between the CR and unCR groups. This non-parametric test evaluates the median differences between two independent samples and was implemented using the function "*ranksu*m" in MATLAB with default parameters.

Effect Size  $r$  for Wilcoxon Rank Sum Test. The  $r$  is calculated as

$$r = \frac{Z}{\sqrt{n}} \quad (2)$$

where  $Z$  is the Z-statistic returned in the "*STATS.zval*" field of the function "*ranksu*m", and  $n$  is the total number of patients ( $N = 23$  here). The effect size is categorized as small (0.1 - 0.3), medium (0.3 - 0.5), and large ( $> 0.5$ )<sup>93</sup>.

For the Fisher Score ranking, each feature's discriminative power was quantified using the formula<sup>94</sup>:

$$FS_i = \frac{\sum_{j=1}^c n_j (\mu_{ij} - \mu_i)^2}{\sum_{j=1}^c n_j \sigma_{ij}^2} \quad (3)$$

where  $c = 2$ , representing the number of classes (CR and unCR),  $n_j$  the number of samples in class  $j$  (8 for CR and 15 for unCR),  $\mu_i$  the overall mean of the  $i$ -th CeTh feature,  $\mu_{ij}$  the mean of the  $i$ -th CeTh feature within class  $j$ , and  $\sigma_{ij}^2$  the variance within class  $j$ , calculated as:

$$\sigma_{ij}^2 = \frac{1}{n_j} \sum_{k=1}^{n_j} (x_{ijk} - \mu_{ij})^2 \quad (4)$$

where  $x_{ijk}$  is the value of the  $i$ -th feature for the  $k$ -th patient in class  $j$ . The Fisher Score was implemented using a custom MATLAB function named “*func\_FisherScore*” provided in the Code availability<sup>95</sup>.

**Step 3 embedded feature selection.** This approach integrates the selection process directly within the classifier algorithm itself, specifically utilizing a model-based feature selection equipped with Lasso regularization (details in the next section). This method inherently penalizes and reduces the weight coefficients of less contributive features, thereby effectively sparsifying feature weights<sup>92,93</sup>. We applied this embedded feature selection technique to four different pathways: (1) The complete set of all 21 cluster-center features without filtering (“Unfiltered”); (2) Features meeting statistical significance criteria, resulting in 6 features (“Sign”); (3) Features with medium to large effect sizes, yielding 11 features (“Effect Size”); (4) Features with high Fisher Scores above the inflection point, producing 5 features (“Fisher Score”). Each of these four pathways underwent the embedded feature selection process independently, yielding distinct weight coefficients for each feature across four pathways.

**Step 4 feature aggregation.** In this step, we combined results from the four feature selection pathways in Step 3. As shown in the Supplementary Fig. 2f, features with model weights above 0.05 were aggregated, leading to the selection of clusters No. 2, No. 6, No. 12, No. 15 and No. 18 (Supplementary Table 2), including six CeTh features: MUAstabilityTheta (stab- $\theta$ ), MUApowerTheta (pow- $\theta$ ), MUApowerAlpha (pow- $\alpha$ ), Firing Rates, syncMUAGamma (sync- $\gamma$ ), and MUAstabilityHGamma (stab-h $\gamma$ ).

**Step 5 wrapper feature selection.** Wrapper methods evaluate various feature subsets to identify the best-performing combination for a specific classifier algorithm. This approach often yields a smaller set of features with strong discriminative power<sup>91,92</sup>. In our study, we iterated over all possible combinations of the six previously identified features, always including stab- $\theta$  (cluster No. 6) due to its significant weight that was much higher than other features (Supplementary Fig. 2f). This iterative process yielded 32 unique feature combinations, each evaluated using the model-based feature selection with L2 regularization (details in the next section, Supplementary Fig. 2g). These 32 combinations were categorized into high accuracy (topAcc, >95% accuracy) and low accuracy (lowAcc) groups. As shown in Supplementary Fig. 2g, the rightmost column displays the Stable-Importance index, which assesses the consistency of a feature’s importance across different combinations in the topAcc group. It is defined as the proportion of combinations where the feature has a weight exceeding a predefined threshold (=0.5):

$$\text{stable - importance}(f) = \frac{N(W_{\text{top}(f)} \geq \text{threshold})}{N(W_{\text{top}(f)})} \quad (5)$$

where  $W_{\text{top}(f)}$  represents the weight vector of feature  $f$  in the topAcc group. It was implemented using a custom MATLAB code provided in the Code availability. A higher proportion indicates a feature’s stable importance, meaning the feature consistently maintains high importance weights across the topAcc group (Supplementary Table 3). The choice of threshold doesn’t significantly affect the ranking of features—

whether set between 0 and 0.43 or 0.47 and 0.72, the top four features with highest stable-importance indices align with the model’s selected features—stab- $\theta$ , sync- $\gamma$ , pow- $\theta$ , and stab-h $\gamma$  (Supplementary Fig. 2h).

Supplementary Table 3 lists each feature’s stable-importance strength along with its average weights in both the topAcc (aveWtop) and lowAcc (aveWlow) groups. Eventually, pow- $\alpha$  and firing rates were excluded from the final optimal feature set (Fig. 1c, right). This exclusion was likely due to their lower stable-importance strength, minimal aveWtop compared to other features, and their own aveWtop being comparatively lower than their aveWlow.

**Model-based feature selection**

It is important to note that our primary objective was to identify a core set of CeTh features that best characterize differences between CR and unCR patients, rather than to develop a generalizable predictive model for clinical use. The machine learning approach described below was used as a methodological tool for feature selection and evaluation. Previous research has shown that machine learning methods can be used to quantify the levels of arousal and awareness in different consciousness states, with classification performance evaluated using nested leave-one-patient-out cross-validation (nested LOPO)<sup>46</sup>.

This nested LOPO method is a variant of leave-one-out cross-validation. In our study, we employed this method combined with a linear Support Vector Machine (SVM) classifier to evaluate the performance of candidate CeTh feature sets for DoC prognosis. Supplementary Fig. 4 illustrates the process of nested LOPO. This process includes inner loops and outer loops, where inner loops are used for hyperparameter tuning and validation, while outer loops are used for final testing. For a dataset with  $N$  patients ( $N = 23$  here), each outer fold is divided as follows: one target patient is selected as the outer test set, and the remaining  $N-1$  patients form the outer training set. Within each outer training set, leave-one-out cross-validation is used again for hyperparameter tuning. The outer training set data is further subdivided, with  $N-2$  participants forming the inner-train set and the remaining one participant used for inner-validation. The model with optimized parameters that minimize validation error is trained on  $N-1$  patients (outer-training) and then tested on the target participant (outer-test). The mean accuracy across outer folds is calculated as the final accuracy of the classification model. Additionally, each outer fold identifies a set of tuned feature weights  $W_i$  (for  $i = 1, 2, \dots, N$ ). We average these  $W_i$ s across all outer folds to obtain the final model importance weights for each feature.

We employed linear SVM as our classification model as our classification model due to its reduced parameter complexity while providing interpretable feature weights. Distinct regularization strategies were applied during different stages of feature selection. In Step 3, Embedded Feature Selection, we utilized Lasso regularization to sparsify model weights. The objective function was:

$$\min_w \sum |w_j| + C \sum \max(0, 1 - y_i w^T x_i)^2 \quad (6)$$

where  $|w_j|$  is the L1 norm of the weight vector inducing sparsity by penalizing the absolute sum of the weights.

In Step 5, L2 regularization was employed with the objective function:

$$\min_w \frac{1}{2} \|w\|^2 + C \sum \max(0, 1 - y_i w^T x_i)^2 \quad (7)$$

where  $\|w\|^2$  is the L2 norm of the weight vector, optimizing performance while preventing overfitting by penalizing the squared sum of weights.

The SVM classification was implemented using the LIBLINEAR package (version 2.43, available at <https://www.csie.ntu.edu.tw/~cjlin/liblinear/>). For Step 3 (L1 regularization), we utilized the L1-regularized

L2-loss support vector classification solver (option “-s 5 -q”), while for Step 5 (L2 regularization), we employed the L2-regularized L2-loss support vector classification solver in its primal form (option “-s 2 -q”).

For hyperparameter tuning, we optimized penalty parameters in our model to determine the optimal balance between model regularization (reducing model complexity and maximizing margin) and misclassification penalty. To address the sample imbalance between CR (8 patients) and unCR (15 patients) groups, we included both the global penalty parameter C and class-specific penalty factors W1 and W2. The global penalty parameter C was tested across a logarithmic range from  $2^{-5}$  to  $2^4$  with incremental steps of  $2^{0.1}$ . For class-specific penalty factors, W1 was kept at 1 while W2 was varied within the range of  $\frac{8}{15} \pm 0.2$  with steps of 0.02. The ratio approximating  $\frac{8}{15}$  was derived from the sample size ratio between the two groups. Thus, the actual implementation of Step 3’s objective function was:

$$\min_w \sum |w_j| + C \cdot W1 \sum_{i \in \{y_i=1\}} \max(0, 1 - y_i w^T x_i)^2 + C \cdot W2 \sum_{i \in \{y_i=-1\}} \max(0, 1 - y_i w^T x_i)^2 \quad (8)$$

Where  $i \in \{y_i=1\}$  corresponds to CR patients, and  $i \in \{y_i=-1\}$  corresponds to unCR patients. Similarly, the actual implementation of Step 5’s objective function was:

$$\min_w \frac{1}{2} \|w\|^2 + C \cdot W1 \sum_{i \in \{y_i=1\}} \max(0, 1 - y_i w^T x_i)^2 + C \cdot W2 \sum_{i \in \{y_i=-1\}} \max(0, 1 - y_i w^T x_i)^2 \quad (9)$$

This approach imposes a higher penalty for misclassifying the minority CR group, helping to mitigate the sample imbalance. Our permutation test results confirm this approach’s effectiveness, with the mean accuracy distributions for permuted datasets appearing at approximately 50%—the expected chance level for binary classification with balanced class samples (Fig. 1d).

The model’s performance in discriminating different patient groups was visualized in the latent features space using both t-Distributed Stochastic Neighbor Embedding (t-SNE) and Principal Component Analysis (PCA). The t-SNE is a non-linear dimensionality reduction technique that preserves local structure by converting similarity relationships into probability distributions and optimized using the Kullback-Leibler divergence. It was implemented using the “tsne” function in MATLAB, initialized with the default parameter, *rng(“default”)* for reproducibility and used the “exact” algorithm for precise computation of joint distributions, applied “euclidean” distance as the metric measuring the distance between patients in the feature space, and set the output to two dimensions using the *Num-Dimensions* parameter. The t-SNE analysis was performed both before and after feature selection to visualize the distribution of patients (CR and unCR) in respective feature spaces. PCA, a linear dimensionality reduction technique, was implemented with the “pca” function in MATLAB. We applied PCA to the post-feature selection data to examine discrimination between patients across different principal components. These visualizations are presented in Supplementary Fig. 3.

**Permutation test**

To validate the robustness of our model accuracy against random chance, we performed a Permutation test. We generated a null distribution by randomly shuffling the patient labels (unCR and CR) 1000 times using the “randperm” function in MATLAB with default settings, creating 1000 permuted datasets. Each permuted dataset was then evaluated using the same classification procedure (SVM plus nested LOPO) that was applied to the actual dataset. The p-value was calculated as the proportion of permuted datasets that achieved accuracy greater than or equal to that obtained with the actual dataset.

Statistical significance was established when the actual classification performance ranked within the top 5% of this null distribution ( $p < 0.05$ ).

**Feature contribution evaluation**

The feature contribution evaluation was conducted to verify the contribution of each feature to the classification performance of the CeTh metric. We sequentially removed features with the smallest weights to demonstrate how each feature improves model performance when included. Starting with all four features, we first removed stab-hy (weight: 11.05). In the next round, we removed sync-γ (weight: 13.44). Then only the two most significant features, stab-θ and pow-θ, remained, with stab-θ ultimately emerging as the top-ranked feature. During this process, accuracy, F1 score, Area Under the Curve (AUC) value of the Receiver Operating Characteristic, Permutation Test p-value, and random baseline accuracy (randAcc) were used to evaluate model performance (Supplementary Table 4).

**F1 score:**

$$\text{Precision} = \frac{TP}{TP + FP} \quad (10)$$

$$\text{Recall} = \frac{TP}{TP + FN} \quad (11)$$

$$F1 - \text{score} = \frac{2 \cdot \text{Precision} \cdot \text{Recall}}{\text{Precision} + \text{Recall}} \quad (12)$$

where true/false positives (TP/FP) and true/false negatives (TN/FN) are used. This metric combines precision and recall to provide a single score that balances both the false positives and false negatives.

**Random baseline accuracy (randACC).** Estimated from the mean accuracy of 1000 shuffled/permuted datasets in the permutation test, this metric provides the model accuracy expected from random binary classification. Specifically, each permuted dataset undergoes the same model-based evaluation process as the actual dataset, serving as a control.

**Feature importance**

Throughout our feature selection pipeline, we assessed feature importance from two views:

- (1) Importance of Single-Feature (Isf): We utilized effect size (r), and Fisher Score ranking to identify features with strong discriminative power between CR and unCR groups.
- (2) Importance in Multi-Feature (Imf): We leveraged both feature weights in the CeTh metric and the Stable-Importance index to measure each feature’s importance and consistent contribution across different feature combinations.

**CeTh metric for DoC prognosis**

We developed a metric based solely on CeTh characteristics, utilizing the selected optimal feature combination and their corresponding model weights (averaged across all folds in the nested LOPO). The formula for the *CeTh metric* is:

$$\text{CeTh metric} = 0.96 \times \text{stab} - \theta + 0.97 \times \text{pow} - \theta + 0.68 \times \text{sync} - \gamma + 0.48 \times \text{stab} - \text{hy} \quad (13)$$

To evaluate the efficacy of this metric, we compared each patient’s decision values as determined by the model with those derived directly from the CeTh metric (Fig. 1f). Our findings demonstrate that the CeTh metric aligned remarkably well with the model classification results, as evidenced by: (1) consistent classification outcomes of all patients (all CR patients above the threshold and all

unCR patients below), and (2) minimal discrepancies between decision values (red lines in Fig. 1f). This consistency indicates that the CeTh metric captures the same discriminative information as the model.

### Subject similarity

Subject similarity was quantified using the reciprocal of the Euclidean distance between each pair of patients in the feature space. Specifically, for two patients,  $P_1$  and  $P_2$ , each characterized by feature vectors  $(F_1, F_2, \dots, F_N)$ , the similarity  $s(P_1, P_2)$  is calculated as follows:

$$s(P_1, P_2) = 1 / \left( \sqrt{(F_{1P_1} - F_{1P_2})^2 + \dots + (F_{NP_1} - F_{NP_2})^2} \right) \quad (14)$$

This similarity score  $s$  was then subjected to min-max normalization across all patient pairs within the subject-similarity matrix to standardize the values. Then we generated similarity matrices comparing CR and unCR patients before feature selection (Supplementary Fig. 5a) and after feature selection (Fig. 2e), as well as among DoC subgroups (I/II/III, Supplementary Fig. 6b). For the CR/unCR patients similarity matrices, we statistically compared the differences between intra-class and inter-class and further examined differences between intra-CR and intra-unCR using the Wilcoxon Rank Sum Test (function “*ranksum*” with default parameters in MATLAB). The results are presented as violin plots (using the *Violinplot-Matlab* package available at <https://github.com/bastibe/Violinplot-Matlab>) as shown in Supplementary Fig. 5b and Fig. 2f. Violin plots display the kernel density estimate of the data distribution (violin shape/width) combined with box plot elements (median, quartiles, and whiskers).

### CeTh-Based DoC subgroups identification

**Identifying DoC subgroups through hierarchical agglomerative clustering.** This methodology, previously leveraged in anesthesia research, has revealed novel patterns of desynchronized neuronal activity, challenging traditionally presumed monotonic correlations between anesthesia depth and neuronal activity<sup>40,95</sup>. Motivated by these findings, we applied hierarchical agglomerative clustering to identify CeTh-based subgroups of DoC, measuring similarities between patients using Euclidean distances based on the CeTh metric. We implemented this using the function “*clustergram*” in MATLAB, setting its properties “*linkage*” parameter to “*weighted*” (WPGMA), “*RowPDist*” parameter to “*spearman*” and “*ColumnPDist*” parameter to “*euclidean*”.

Next, we determined the optimal number of clusters based on the hierarchical clusters and the so-called elbow method<sup>40</sup>. Specifically, from the hierarchical clustering output of MATLAB’s “*linkage*” function (using “*weighted*” method and “*euclidean*” metric), we extracted the between-cluster distance for each merge from  $K+1$  clusters to  $K$  clusters. When this distance value is large, it indicates that the process of clustering from  $K+1$  to  $K$  clusters would actually merge two dissimilar subclusters that are suggested to keep separated. Subsequently, we plotted these distance values (min-max normalized) against the number of clusters (Supplementary Fig. 6a). By calculating the second-order difference of the distance–cluster curve and identifying its maximum value, we identified the elbow point with the greatest curvature, which marks the sharpest shift in distance reduction, thereby determining the cluster number.

In our result, we identified distinct CeTh activity patterns within DoC patients. Based on the elbow method, we selected  $K=4$ , resulting in the formation of four distinct clusters. Subgroups I and II exhibited clear clustering (Fig. 3a and Supplementary Fig. 6b). Among the remaining two clusters, one contained only Patient No. 6. However, relying on a single-patient cluster for subgroup analysis would limit generalizability. Therefore, we analyzed the distance between Patient No. 6 and the other three clusters separately to determine its most similar cluster. Specifically, we calculated the subject similarity (the

reciprocal of the Euclidean distance described above) between Patient No. 6 and each patient in subgroup I, then obtained the mean similarity value of 0.36 as the overall similarity between Patient No. 6 and subgroup I. Similarly, the similarity between Patient No. 6 and subgroup II was 0.42. Patient No. 6 and the third remaining cluster shared the highest similarity value of 0.45. Moreover, this strongest similarity was particularly evident in the *stab-θ* feature (Fig. 3a and Supplementary Fig. 6c), which we identified as the most critical CeTh feature in the “Feature contribution evaluation” section (Supplementary Table 4). Therefore, No.6 and this remaining cluster were merged into Subgroup III. It helps avoid drawing conclusions from a single-patient cluster that might reflect individual variability rather than a representative neurophysiological pattern, while maintaining coherence in key electrophysiological features. The distributions of CeTh features across patients were illustrated by a radar chart (adapted from the package available at <https://www.mathworks.com/matlabcentral/fileexchange/126450-radar-chart> with “*Type*” parameter set to “*Patch*”) as shown in the Supplementary Fig. 6c.

**Venn diagram analysis of feature combinations.** For each patient, a feature was categorized as high-value if its value exceeded the median value of the entire group. We analyzed the distribution of these high-value features within each DoC group using Venn diagrams (Fig. 2g, h and Fig. 3c–e). To address potential sample imbalances among the DoC groups (CR/unCR or Subgroups I/II/III), we implemented oversampling with replacement to balance the classes. This was achieved by resampling each group to match the size of the largest group (using the *randsample* function in MATLAB with the “*Replace*” parameter set to “*true*”), followed by repeating this process 1000 times to accurately obtain the distribution of CeTh features among these groups<sup>96</sup>. The averaged results from these resampling iterations were used to construct the final Venn diagrams (adapted from the package available at <https://www.mathworks.com/matlabcentral/fileexchange/116760-venn-diagram>). Additionally, the accompanying pie charts illustrate the distribution of patients based on the number of simultaneously high-value features. These charts were generated using the function “*pie*” in MATLAB with the “*explode*” parameter set to properly space the labels. The pie charts show the percentage of patients with different numbers of high-value features (FN), including patients with no high-value features (FN=0), only one high-value feature (FN=1), or with two, three, or four high-value features simultaneously (FN=2/3/4).

### Biophysical simulation model

**Model overview.** Our model simulated interactions between inhibitory neurons within the thalamic reticular nucleus (TRN) and excitatory neurons in the thalamocortical relay nuclei<sup>97,98</sup>. Following established thalamic organization<sup>55,99,100</sup>, these excitatory neurons included two types: matrix neurons in non-specific relay nuclei (i.e., CeTh here) and core neurons in specific relay nuclei (SR). This three-component thalamic configuration (TRN, SR, and CeTh) is commonly employed in computational studies of anesthesia-induced LOC<sup>101</sup> and thalamocortical dysrhythmia<sup>57</sup>. Thus, our study simulated TRN, CeTh, and SR, each with 100 neurons.

**Input and connectivity.** Each neuron received random excitatory input modeled by a Poisson spike train with a base discharge probability  $P$  of 0.5 for CeTh/SR and 0.15 for TRN<sup>57</sup>. Connectivity was established with one-to-one connections between SP and TRN and one-to-many connections from CeTh to TRN at a probability of 0.15<sup>57,97</sup>. Additional connectivity details are provided in Supplementary Table 5.

**Neuron dynamics.** Neuron dynamics were modeled using the integrate-and-fire-or-burst approach<sup>102</sup>, adapting the classical conductance-based leaky integrate-and-fire model to include low-

threshold bursting (LTB) (Eqs. 15–17). This adaptation was critical for simulating thalamic discharge patterns under deafferentation conditions, essential for understanding thalamocortical rhythmic activities. Parameters related to thalamic neuronal dynamics are outlined in Supplementary Table 6.

**Model equations.** The membrane potential  $V$  of neurons is modeled by:

$$C \frac{dV}{dt} = I_{in} - I_L - I_T \quad (15)$$

where  $C$  is the membrane capacitance,  $I_{in}$  represents the synaptic input current,  $I_L$  is the leak current, and  $I_T$  is the total calcium current. Neurons spike when  $V$  exceeds a threshold  $V_\theta$ , after which it is reset to  $V_{reset}$ .

The synaptic input current  $I_{in}$  is derived from the sum of excitatory and inhibitory synaptic currents:

$$I_{in} = (E_{exc} - V) \sum_i g_{E_i} + (E_{inh} - V) \sum_j g_{I_j} \quad (16)$$

where  $E_{exc}$  and  $E_{inh}$  represent the excitatory and inhibitory reversal potentials, respectively, and  $g_{E_i}$  and  $g_{I_j}$  are the conductances for excitatory and inhibitory synapses.

Synaptic conductance decays exponentially with a time constant  $\tau_s$ , modulated by presynaptic firing events after a connection-specific delay. Specifically, when a presynaptic neuron fires, it causes a temporary increase in synaptic conductance by  $g_{E/I}$ , which then follows an exponential decay:

$$\frac{dg_{E/I}}{dt} = -\frac{g_{E/I}}{\tau_s} + \delta(t - t_{delay}) g_s \quad (17)$$

In this equation,  $\delta(t - t_{delay})$  represents a delta function that activates at the delay time  $t_{delay}$  following presynaptic firing.

The leak current  $I_L$  is defined by:

$$I_L = g_L (V - E_L) \quad (18)$$

with  $g_L$  as the leak conductance and  $E_L$  the leak reversal potential.

As DoC is associated with a reduced neuronal resting membrane potential (RMP) due to potassium leakage currents<sup>9,58,59</sup>, a lower RMP is set for simulating DoC conditions. This RMP is lower than both the healthy RMP and the calcium LTB threshold.

The calcium current,  $I_T$ , is critically dependent on the inactivation state  $h$  and is governed by the equation:

$$I_T = g_T m_\infty h (V - E_T) \quad (19)$$

Here,  $g_T$  is the calcium conductance,  $E_T$  is the calcium reversal potential, and  $m_\infty$  is defined by the heaviside step function  $H$ , as follows:

$$m_\infty = H(V - V_h) \quad (20)$$

This function ensures that activation occurs instantaneously above a threshold voltage  $V_h$ . The inactivation variable  $h$  dynamically adjusts based on the membrane potential  $V$ , engaging in a two-stage de-inactivation–activation process. This process allows  $h$  to approach zero when  $V$  exceeds  $V_h$  (depolarized conditions) and to approach one under hyperpolarized conditions, with transitions governed by specific time constants  $\tau_h^-$  and  $\tau_h^+$ :

$$\frac{dh}{dt} = \begin{cases} -h/\tau_h^- & (V > V_h) \\ (1-h)/\tau_h^+ & (V < V_h) \end{cases} \quad (21)$$

**Modeling various afferent conditions.** The deafferentation in our simulation primarily represents a reduction in excitatory inputs from corticothalamic axons (originating from layer 5 and/or layer 6 neurons) to the thalamocortical relay cells (both SR and CeTh, but not TRN)<sup>30,99</sup>. Varied levels of structural and functional deafferentation were modeled through different afferent conditions, encompassing three main factors:

- (1) Proportion of deafferented neurons (deaffRatio): this parameter represents the percentage of neurons undergoing deafferentation, with values ranging from 0 to 100%. If there is no residual input left, i.e., complete deafferentation, it leads to an absence of discharging activity, simulating conditions akin to neuronal damage per se within the network.
- (2) Afferent magnitude (affMag) of residual input: this factor adjusts the magnitude of residual input preserved in neurons that have undergone partial reafferentiation (Fig. 5a). The afferent magnitude (affMag) varies from 0 to 100% relative to normal spike train input conditions (discharge probability  $P$  of 0.5 for the CeTh neurons).
- (3) Afferent stability (affStab) of residual input: stability is manipulated by introducing “silent periods” that intermittently suppress the input spike train (Fig. 5a). This approach models alternating phases of normal activity and “silent periods” for all neurons to simulate intermittent spiking inputs under slow oscillation and/or burst suppression, which can significantly alter the overall membrane potentials across CeTh neurons. The impact of these “silent periods” on input stability is quantified from 0% (complete suppression during “silent periods”) to 100% (full preservation of spikes during “silent periods”). For instance, an affStab of 50% means that during “silent periods”, half of the expected input spikes are lost compared to normal conditions.

**Four afferent input stages.** Our simulations delineated four distinct stages based on various afferent conditions:

**Stage I.** Most CeTh neurons (deaffRatio  $\geq 90\%$ ) are under complete deafferentation, exhibiting a quiescent state.

**Stage II.** Partial restoration in completely deafferented CeTh neurons (reducing deaffRatio to 30%) leads to slightly higher firing rates than Stage I but remains insufficient to produce theta rhythms.

**Stage III.** The impaired CeTh neurons undergo reafferentiation by restoring certain residual afferent inputs. This induces a theta rhythmic state, with the strongest theta rhythm under a setting of affMag of 4%.

**Stage IV.** All CeTh neurons are fully restored to a healthy profile, with complete reafferentiation (deaffRatio = 0% and affMag = 100%), and membrane potential restored to normal RMP.

**Analysis of simulated CeTh activities.** To analyze the simulated CeTh activities, we first calculated the firing rates by averaging the number of spikes per second across all CeTh neurons. Subsequently, we averaged the membrane potentials of all CeTh neurons at each timestep, beginning three seconds post-initiation. This averaged data provided the foundation for further analysis, including:

**Power and stability assessment.** We evaluated pow- $\theta$  and stab- $\theta$  using methodologies consistent with those applied to empirical MUA signals, including normalized power and signal stability for MUA activity in the theta band (details in the “Signal processing and feature extraction” section). Notably, compared to LFP—a proxy for synaptic input—MUA provides more localized information regarding population outputs<sup>35,36</sup>. Thus, in this context, the simulation model that

describes the rhythmic activity of CeTh outputs (small size nuclei) more closely aligns with the rhythms observed in MUA.

**Power spectral density (PSD).** The PSD of CeTh activities was calculated to capture frequency components ranging from 0 to 80 Hz.

### Statistical analysis

Besides the previously described Wilcoxon Rank Sum Test, Pearson Correlation, Spearman Correlation and Permutation Test, our study employed several other statistical methods for additional analysis:

**Fisher's exact test.** To evaluate the statistical independence between categorical variables, we employed Fisher's Exact Test, particularly useful for small datasets when expected frequencies in any cells of a contingency table are below 5. For binary comparisons (between UWS and MCS- groups, younger and older groups, between any two subgroups), we used the standard Fisher's Exact Test. For scenarios involving three categories (comparisons among three etiologies and three subgroups), we utilized an extended version of Fisher's Exact Test. This adaptation accommodates larger contingency tables through a network algorithm for exact computation of p-values, effectively handling more complex categorical relationships. Both the standard and extended tests were implemented using the *"fisher.test"* function (package *"stats"*) in R with default parameters.

**Odds ratio (OR).** Implemented by the conditional maximum likelihood estimate using the *"fisher.test"* function (package *"stats"*) in R with default parameters, quantifying the strength and direction of the association between two categorical variables. This approach is particularly suited for small sample sizes or unevenly distributed categorical data, ensuring robust and unbiased estimates of association strength. An OR greater than 1 indicates a positive association, less than 1 indicates a negative association, and equal to 1 indicates no association.

**Effect size (Cohen's h).** To quantify the magnitude of association between the two categorical variables, we calculated Cohen's h, defined as:

$$h = 2 \times \left( \arcsin(\sqrt{p1}) - \arcsin(\sqrt{p2}) \right) \quad (22)$$

where  $p1$  and  $p2$  are the proportions from two independent groups. The effect size was implemented using a custom function in R. This approach was used to assess proportional differences between groups, such as the CR ratio between young and older patients and the recovery ratio between different subgroups.

**Kruskal-Wallis (KW) test.** We used this test to assess statistical differences in CeTh features among various etiologies, followed by a post-hoc analysis using Conover's All-Pairs Rank Comparison Test. The KW test was implemented using the *"kruskalTest"* function (package *"PMCMRplus"*) with *"dist"* parameter set to *"FDist"* in R. Its post-hoc analysis for pairwise comparisons was performed using Conover's all-pairs test, implemented with the *"kwAllPairsConoverTest"* function (package *"PMCMRplus"*) with *"p.adjust.method"* set to *"none"* in R.

**Effect size ( $\eta^2$ ).** The effect size for the KW test was calculated as<sup>103</sup>:

$$\eta^2 = \frac{F \cdot (k - 1)}{F \cdot (k - 1) + (N - k)} \quad (23)$$

where  $N$  was the sample size,  $k$  was the number of groups, and  $F$  was the F-statistic obtained from the *"kruskalTest"* function output. In our analysis of CeTh features across different etiologies, we used  $k = 3$  (representing three etiological groups) with a total sample size of  $N = 23$ .

**Significance level.** Significance levels are represented as follows: no significance (n.s.) for  $p \geq 0.05$ ; \* for  $p < 0.05$ ; \*\* for  $p < 0.01$ ; \*\*\* for  $p < 0.001$ .

All data preprocessing and analyses were conducted using MATLAB R2023 (MathWorks, Inc.) and RStudio (R 4.3.2).

### Reporting summary

Further information on research design is available in the Nature Portfolio Reporting Summary linked to this article.

### Data availability

The processed electrophysiological data used to generate results in this study are provided in the Source Data file. The raw electrophysiological data are available under restricted access due to patient privacy and ethical considerations. Access requests directed to the corresponding author (S.Y., shan.yu@nlpr.ia.ac.cn and J.H.H., he.jianghong@sina.cn) with institutional affiliation verification for legitimate research purposes and appropriate data use agreements. Requests will be reviewed within 30 days and data will be shared under appropriate data use agreements that ensure patient privacy protection. Source data are provided with this paper.

### Code availability

Custom code associated with this study is available at <https://github.com/HRZ-Sim/DoC-CeTh-2025>, and has been deposited in Zenodo (<https://doi.org/10.5281/zenodo.17060496>).

### References

1. Teasdale, G. & Jennett, B. Assessment of coma and impaired consciousness. A practical scale. *Lancet* **2**, 81–84 (1974).
2. Jennett, B. & Plum, F. Persistent vegetative state after brain damage. A syndrome in search of a name. *Lancet* **1**, 734–737 (1972).
3. Multi-Society Task Force on PVS, Medical aspects of the persistent vegetative state. *N. Engl. J. Med.* **330**, 1499–1508 (1994).
4. Laureys, S. et al. Unresponsive wakefulness syndrome: a new name for the vegetative state or apallic syndrome. *BMC Med.* **8**, 68 (2010).
5. Giacino, J. T. et al. The minimally conscious state: definition and diagnostic criteria. *Neurology* **58**, 349–353 (2002).
6. Laureys, S., Gosseries, O. & Tononi, G. *The Neurology of Consciousness: Cognitive Neuroscience and Neuropathology* (Academic Press, 2015).
7. Thibaut, A., Bodien, Y. G., Laureys, S. & Giacino, J. T. Minimally conscious state "plus": diagnostic criteria and relation to functional recovery. *J. Neurol.* **267**, 1245–1254 (2020).
8. Bernat, J. L. Chronic disorders of consciousness. *Lancet* **367**, 1181–1192 (2006).
9. Edlow, B. L., Claassen, J., Schiff, N. D. & Greer, D. M. Recovery from disorders of consciousness: mechanisms, prognosis and emerging therapies. *Nat. Rev. Neurol.* **17**, 135–156 (2021).
10. Estraneo, A. et al. Late recovery after traumatic, anoxic, or hemorrhagic long-lasting vegetative state. *Neurology* **75**, 239–245 (2010).
11. Yamamoto, T. et al. Deep brain stimulation for the treatment of vegetative state. *Eur. J. Neurosci.* **32**, 1145–1151 (2010).
12. Chudy, D. et al. Deep brain stimulation for the early treatment of the minimally conscious state and vegetative state: experience in 14 patients. *J. Neurosurg.* **128**, 1189–1198 (2018).
13. Yang, Y. et al. Long-term functional outcomes improved with deep brain stimulation in patients with disorders of consciousness. *Stroke Vasc. Neurol.* **8**, 368–378 (2023).
14. Schiff, N. D. et al. Behavioural improvements with thalamic stimulation after severe traumatic brain injury. *Nature* **448**, 600–603 (2007).

15. Song, M. et al. Prognostic models for prolonged disorders of consciousness: an integrative review. *Cell. Mol. Life Sci.* **77**, 3945–3961 (2020).
16. Laureys, S. et al. Restoration of thalamocortical connectivity after recovery from persistent vegetative state. *Lancet* **355**, 1790–1791 (2000).
17. Song, M. et al. Prognostication of chronic disorders of consciousness using brain functional networks and clinical characteristics. *Elife* **7**, e36173 (2018).
18. Vanhaudenhuyse, A. et al. Default network connectivity reflects the level of consciousness in non-communicative brain-damaged patients. *Brain* **133**, 161–171 (2010).
19. Sitt, J. D. et al. Large scale screening of neural signatures of consciousness in patients in a vegetative or minimally conscious state. *Brain* **137**, 2258–2270 (2014).
20. Chennu, S. et al. Brain networks predict metabolism, diagnosis and prognosis at the bedside in disorders of consciousness. *Brain* **140**, 2120–2132 (2017).
21. Engemann, D. A. et al. Robust EEG-based cross-site and cross-protocol classification of states of consciousness. *Brain* **141**, 3179–3192 (2018).
22. Sadikot, A. F. & Rymar, V. V. The primate centromedian-parafascicular complex: Anatomical organization with a note on neuromodulation. *Brain Res. Bull.* **78**, 122–130 (2009).
23. Groenewegen, H. J. & Berendse, H. W. The specificity of the ‘nonspecific’ midline and intralaminar thalamic nuclei. *Trends Neurosci.* **17**, 52–57 (1994).
24. Rholp, P. et al. Arousal-revisiting the reticular activating system. *Science* **272**, 225–226 (1996).
25. Baker, J. L. et al. Robust modulation of arousal regulation, performance, and frontostriatal activity through central thalamic deep brain stimulation in healthy nonhuman primates. *J. Neurophysiol.* **116**, 2383–2404 (2016).
26. Redinbaugh, M. J. et al. Thalamus modulates consciousness via layer-specific control of cortex. *Neuron* **106**, 66–75.e12 (2020).
27. Bastos, A. M. et al. Neural effects of propofol-induced unconsciousness and its reversal using thalamic stimulation. *Elife* **10**, e60824 (2021).
28. Tasserie, J. et al. Deep brain stimulation of the thalamus restores signatures of consciousness in a nonhuman primate model. *Sci. Adv.* **8**, eabl5547 (2022).
29. Arnts, H. et al. The intralaminar thalamus: a review of its role as a target in functional neurosurgery. *Brain Commun.* **5**, fcad003 (2023).
30. Whyte, C. J., Redinbaugh, M. J., Shine, J. M. & Saalman, Y. B. Thalamic contributions to the state and contents of consciousness. *Neuron* **112**, 1611–1625 (2024).
31. Giacino, J., Fins, J. J., MacHado, A. & Schiff, N. D. Central thalamic deep brain stimulation to promote recovery from chronic post-traumatic minimally conscious state: Challenges and opportunities. *Neuromodulation* **15**, 339–349 (2012).
32. Magrassi, L. et al. Single unit activities recorded in the thalamus and the overlying parietal cortex of subjects affected by disorders of consciousness. *PLoS ONE* **13**, 1–17 (2018).
33. He, J. et al. Electrophysiological characteristics of CM-pf in diagnosis and outcome of patients with disorders of consciousness. *Brain Stimul.* **16**, 1522–1532 (2023).
34. Kajikawa, Y. & Schroeder, C. E. How local is the local field potential? *Neuron* **72**, 847–858 (2011).
35. Buzsáki, G. Large-scale recording of neuronal ensembles. *Nat. Neurosci.* **7**, 446–451 (2004).
36. Stark, E. & Abeles, M. Predicting movement from multiunit activity. *J. Neurosci.* **27**, 8387–8394 (2007).
37. Mattia, M., Ferraina, S. & Del Giudice, P. Dissociated multi-unit activity and local field potentials: a theory inspired analysis of a motor decision task. *Neuroimage* **52**, 812–823 (2010).
38. Georgiades, M. J. et al. Hitting the brakes: pathological sub-thalamic nucleus activity in Parkinson’s disease gait freezing. *Brain* **142**, 3906–3916 (2019).
39. Georgiades, M. J. et al. Subthalamic nucleus activity during cognitive load and Gait dysfunction in Parkinson’s disease. *Mov. Disord.* **38**, 1549–1554 (2023).
40. Lee, H., Wang, S. & Hudetz, A. G. State-dependent cortical unit activity reflects dynamic brain state transitions in anesthesia. *J. Neurosci.* **40**, 9440–9454 (2020).
41. Zhang, Y., Li, Z., Dong, H. & Yu, T. Effects of general anesthesia with propofol on thalamocortical sensory processing in rats. *J. Pharm. Sci.* **126**, 370–381 (2014).
42. Fries, P., Womelsdorf, T., Oostenveld, R. & Desimone, R. The effects of visual stimulation and selective visual attention on rhythmic neuronal synchronization in macaque area V4. *J. Neurosci.* **28**, 4823 (2008).
43. Gregoriou, G. G., Gots, S. J., Zhou, H. & Desimone, R. High-Frequency, long-range coupling between prefrontal and visual cortex during attention. *Science* **324**, 1207–1210 (2009).
44. Warren, A. E. L. et al. Targeting the centromedian thalamic nucleus for deep brain stimulation. *J. Neurol. Neurosurg. Psychiatry* **91**, 339–349 (2020).
45. Luppi, A. I. et al. Computational modelling in disorders of consciousness: closing the gap towards personalised models for restoring consciousness. *Neuroimage* **275**, 20162 (2023).
46. Lee, M. et al. Quantifying arousal and awareness in altered states of consciousness using interpretable deep learning. *Nat. Commun.* **13**, 1–14 (2022).
47. Brown, E. N., Lydic, R. & Schiff, N. D. General anesthesia, sleep, and coma. *N. Engl. J. Med.* **363**, 2638–2650 (2010).
48. Destexhe, A. & Sejnowski, T. J. Interactions between membrane conductances underlying thalamocortical slow-wave oscillations. *Physiol. Rev.* **83**, 1401–1453 (2003).
49. Linás, R. R. & Steriade, M. Bursting of thalamic neurons and states of vigilance. *J. Neurophysiol.* **95**, 3297–3308 (2006).
50. Llinás, R., Urbano, F. J., Leznik, E., Ramírez, R. R. & Van Marle, H. J. F. Rhythmic and dysrhythmic thalamocortical dynamics: GABA systems and the edge effect. *Trends Neurosci.* **28**, 325–333 (2005).
51. Vanneste, S., Song, J.-J. & De Ridder, D. Thalamocortical dysrhythmia detected by machine learning. *Nat. Commun.* **9**, 1103 (2018).
52. Jeanmonod, D., Magnin, M. & Morel, A. Low-threshold calcium spike bursts in the human thalamus: common physiopathology for sensory, motor and limbic positive symptoms. *Brain* **119**, 363–375 (1996).
53. Crunelli, V. et al. Dual function of thalamic low-vigilance state oscillations: Rhythm-regulation and plasticity. *Nat. Rev. Neurosci.* **19**, 107–118 (2018).
54. Lewis, L. D. et al. Thalamic reticular nucleus induces fast and local modulation of arousal state. *Elife* **4**, e08760 (2015).
55. Jones, E. G. The thalamic matrix and thalamocortical synchrony. *Trends Neurosci.* **24**, 595–601 (2001).
56. Müller, E. J. et al. Core and matrix thalamic sub-populations relate to spatio-temporal cortical connectivity gradients. *Neuroimage* **222**, 117224 (2020).
57. Henning Proske, J., Jeanmonod, D. & Verschure, P. F. M. J. A computational model of thalamocortical dysrhythmia. *Eur. J. Neurosci.* **33**, 1281–1290 (2011).
58. Monti, M. M. & Sannita, W. G. *Brain Function and Responsiveness in Disorders of Consciousness* (Springer International Publishing, 2016).
59. Schiff, N. D. Recovery of consciousness after brain injury: a mesocircuit hypothesis. *Trends Neurosci.* **33**, 1–9 (2010).

60. Steyn-Ross, D. A., Steyn-Ross, M. L., Sleigh, J. W. & Wilson, M. T. Progress in modeling EEG effects of general anesthesia: biphasic response and hysteresis. in (ed. Hutt, A.) *Sleep and Anesthesia*, 167–194 (Springer, 2011).
61. Honjoh, S. et al. Regulation of cortical activity and arousal by the matrix cells of the ventromedial thalamic nucleus. *Nat. Commun.* **9**, 2100 (2018).
62. Massimini, M. et al. Triggering sleep slow waves by transcranial magnetic stimulation. *Proc. Natl. Acad. Sci. USA* **104**, 8496–8501 (2007).
63. Takahashi, S. et al. Hypoxic brain damage: cortical laminar necrosis and delayed changes in white matter at sequential MR imaging. *Radiology* **189**, 449–456 (1993).
64. Mohamed, A. Z. et al. Evaluating spatiotemporal microstructural alterations following diffuse traumatic brain injury. *Neuroimage Clin.* **25**, 102136 (2020).
65. Edlow, B. L. et al. Early detection of consciousness in patients with acute severe traumatic brain injury. *Brain* **140**, 2399–2414 (2017).
66. Schnakers, C. et al. Diagnostic accuracy of the vegetative and minimally conscious state: clinical consensus versus standardized neurobehavioral assessment. *BMC Neurol.* **9**, 1–5 (2009).
67. Owen, A. M. et al. Detecting awareness in the vegetative state. *Science* **313**, 1402 (2006).
68. Monti, M. M. et al. Willful modulation of brain activity in disorders of consciousness. *N. Engl. J. Med.* **362**, 579–589 (2010).
69. Kondziella, D. et al. European Academy of Neurology guideline on the diagnosis of coma and other disorders of consciousness. *Eur. J. Neurol.* **2020**, 741–756 (2020).
70. Barra, M. E. et al. Common data elements for disorders of consciousness: recommendations from the working group on hospital course, confounders, and medications. *Neurocrit. Care* **39**, 586–592 (2023).
71. Kondziella, D., Friberg, C. K., Frokjaer, V. G., Fabricius, M. & Møller, K. Preserved consciousness in vegetative and minimal conscious states: systematic review and meta-analysis. *J. Neurol. Neurosurg. Psychiatry* **87**, 485–492 (2016).
72. Lukatch, H. S. & MacIver, M. B. Synaptic mechanisms of thiopental-induced alterations in synchronized cortical activity. *Anesthesiology* **84**, 1425–1434 (1996).
73. Lukatch, H. S., Kiddoo, C. E. & MacIver, M. B. Anesthetic-induced burst suppression eeg activity requires glutamate-mediated excitatory synaptic transmission. *Cereb. Cortex* **15**, 1322–1331 (2005).
74. Clark, D. L. & Rosner, B. S. Neurophysiologic effects of general anesthetics. I. The electroencephalogram and sensory evoked responses in man. *Anesthesiology* **38**, 564–582 (1973).
75. Pinault, D. Cellular interactions in the rat somatosensory thalamocortical system during normal epileptic 5–9 Hz oscillations. *J. Physiol.* **552**, 881–905 (2003).
76. Schiff, N. D. Mesocircuit mechanisms in the diagnosis and treatment of disorders of consciousness. *Presse Med.* **52**, 104161 (2023).
77. Amico, E. et al. Mapping the functional connectome traits of levels of consciousness. *Neuroimage* **148**, 201–211 (2017).
78. Boly, M. et al. Preserved feedforward but impaired top-down processes in the vegetative state. *Science* **332**, 858–862 (2011).
79. Wang, H. et al. Thalamic burst and tonic firing selectively indicate patients' consciousness level and recovery. *Innovation* **6**, 100846 (2025).
80. Schiff, N. D. et al. Thalamic deep brain stimulation in traumatic brain injury: a phase 1, randomized feasibility study. *Nat. Med.* **29**, 3162–3174 (2023).
81. Flores, F. J. et al. Thalamocortical synchronization during induction and emergence from propofol-induced unconsciousness. *Proc. Natl. Acad. Sci. USA* **114**, E6660–E6668 (2017).
82. Rosanova, M. et al. Natural frequencies of human corticothalamic circuits. *J. Neurosci.* **29**, 7679–7685 (2009).
83. Monti, M. M. et al. Thalamo-frontal connectivity mediates top-down cognitive functions in disorders of consciousness. *Neurology* **84**, 167–173 (2015).
84. Edlow, B. L. et al. Therapies to restore consciousness in patients with severe brain injuries: a gap analysis and future directions. *Neurocrit. Care* **35**, 68 (2021).
85. Dolan, K., Martens, H. C. F., Schuurman, P. R. & Bour, L. J. Automatic noise-level detection for extra-cellular micro-electrode recordings. *Med. Biol. Eng. Comput.* **47**, 791–800 (2009).
86. Abeles, M. & Goldstein, M. H. Multispikes train analysis. *Proc. IEEE* **65**, 762–773 (1977).
87. Ziemba, C. M. et al. Laminar differences in responses to naturalistic texture in macaque V1 and V2. *J. Neurosci.* **39**, 9748–9756 (2019).
88. Supèr, H. & Roelfsema, P. R. Chronic multiunit recordings in behaving animals: advantages and limitations. *Prog. Brain Res.* **147**, 263–282 (2005).
89. Vega-Zelaya, L., Torres, C. V., Navas, M. & Pastor, J. Neurophysiological characterization of thalamic nuclei in epileptic anaesthetized patients. *Brain Sci.* **9**, 1–16 (2019).
90. Campbell, M. J. & Swinscow, T. D. V. Statistics at square one. *Br. Med. J.* **1**, 1240 (1976).
91. Saeys, Y., Inza, I. & Larrañaga, P. A review of feature selection techniques in bioinformatics. *Bioinformatics* **23**, 2507–2517 (2007).
92. Guyon, I. & De, A. M. An introduction to variable and feature selection André Elisseeff. *J. Mach. Learn. Res.* **3**, 1157–1182 (2003).
93. Cohen, J. *Statistical Power Analysis for the Behavioral Sciences*, 2nd edn (Routledge, 1988).
94. Zhang, J. et al. FS-GBDT: identification multicancer-risk module via a feature selection algorithm by integrating Fisher score and GBDT. *Brief. Bioinform.* **22**, 1–13 (2021).
95. Hudson, A. E., Calderon, D. P., Pfaff, D. W. & Proekt, A. Recovery of consciousness is mediated by a network of discrete metastable activity states. *Proc. Natl. Acad. Sci. USA* **111**, 9283–9288 (2014).
96. Steyerberg, E. W. *Clinical Prediction Models: a Practical Approach to Development, Validation*. Springer Science & Business Media (John Wiley & Sons, Ltd, 2008).
97. Steriade, M. & Deschenes, M. The thalamus as a neuronal oscillator. *Brain Res. Rev.* **8**, 1–63 (1984).
98. Murray Sherman, S. & Guillery, R. W. *Exploring the Thalamus and Its Role in Cortical Function*, 2nd edn (MIT Press, 2006).
99. Ribary, U., Doesburg, S. M. & Ward, L. M. Unified principles of thalamocortical network dynamics: a framework for typical/atypical functional connectivity. in *Magnetoencephalography*, 1–28 (Springer, 2019).
100. Jones, E. G. Synchrony in the interconnected circuitry of the thalamus and cerebral cortex. *Ann. N. Y. Acad. Sci.* **1157**, 10–23 (2009).
101. Müller, E. J. et al. The non-specific matrix thalamus facilitates the cortical information processing modes relevant for conscious awareness. *Cell Rep.* **42**, 112844 (2023).
102. Smith, G. D., Cox, C. L., Sherman, S. M. & Rinzal, J. Fourier analysis of sinusoidally driven thalamocortical relay neurons and a minimal integrate-and-fire-or-burst model. *J. Neurophysiol.* **83**, 588–610 (2000).
103. Richardson, J. T. E. Eta squared and partial eta squared as measures of effect size in educational research. *Educ. Res. Rev.* **6**, 135–147 (2011).
104. Sherman, S. M. & Guillery, R. W. *Functional connections of cortical areas: a new view from the thalamus* (MIT Press, 2013).

## Acknowledgements

We thank Binghao Yang and Shenghao Cao for technical help. We thank Chiara Cirelli and Ruoshui Xu for helpful discussions. We thank Shuai Han, Xiaoli Geng and Xueling Chen for clinical professional assistance during clinical data collection and patient management. This work was supported by the National Key Research and Development Program (2023YFB4706100), National Natural Science Foundation of China (82272118), and Beijing Natural Science Foundation (7232046) to J.H.H.; and by the National Key R&D Program of China (2022YFE0141300), Canada Excellence Research Chair in Neuroplasticity, European Foundation of Biomedical Research FERB Onlus, fund Generet of King Baudouin Foundation, Mind Care International Foundation to S.L. S.L. is Honorary Research Director at the Belgian National Fund for Scientific Research (FRS-FNRS).

## Author contributions

Conceptualization: H.R.Z., S.Y., and J.H.H. Resources: J.H.H., Q.Q.G., L.X., Y.Y.D., and Y.T.Z. Methodology: H.R.Z., S.Y., Q.Q.G., J.H.H., X.L., and S.W. Investigation: H.R.Z., S.Y., J.H.H., Q.Q.G., X.L., S.L., S.W., L.X., Y.Y.D., and Y.T.Z. Visualization: H.R.Z., S.Y., Q.Q.G., J.H.H., S.L., and X.L. Funding acquisition: J.H.H., S.Y., and S.L. Project administration and Supervision: J.H.H. and S.Y. Writing—original draft: H.R.Z., S.Y., Q.Q.G., and J.H.H. Writing—review & editing: H.R.Z., S.Y., Q.Q.G., J.H.H., and S.L.

## Competing interests

The authors declare no competing interests.

## Additional information

**Supplementary information** The online version contains supplementary material available at <https://doi.org/10.1038/s41467-025-65360-4>.

**Correspondence** and requests for materials should be addressed to Steven Laureys, Jianghong He or Shan Yu.

**Peer review information** *Nature Communications* thanks Julia Sophia Crone, Didier Pinault, Alik Widge and the other, anonymous, reviewer(s) for their contribution to the peer review of this work. A peer review file is available.

**Reprints and permissions information** is available at <http://www.nature.com/reprints>

**Publisher's note** Springer Nature remains neutral with regard to jurisdictional claims in published maps and institutional affiliations.

**Open Access** This article is licensed under a Creative Commons Attribution-NonCommercial-NoDerivatives 4.0 International License, which permits any non-commercial use, sharing, distribution and reproduction in any medium or format, as long as you give appropriate credit to the original author(s) and the source, provide a link to the Creative Commons licence, and indicate if you modified the licensed material. You do not have permission under this licence to share adapted material derived from this article or parts of it. The images or other third party material in this article are included in the article's Creative Commons licence, unless indicated otherwise in a credit line to the material. If material is not included in the article's Creative Commons licence and your intended use is not permitted by statutory regulation or exceeds the permitted use, you will need to obtain permission directly from the copyright holder. To view a copy of this licence, visit <http://creativecommons.org/licenses/by-nc-nd/4.0/>.

© The Author(s) 2025